Catalysis
Science &
Technology

ROYAL SOCIETY
OF CHEMISTRY

REVIEW

View Article Online
View Journal | View Issue

Cite this: *Catal. Sci. Technol.*, 2025, **15**, 6976

A review on MXene modified quantum dot photocatalysts for sustainable energy generation and environmental remediation

Prativa Das, Lijarani Biswal and Kulamani Parida*

Received 20th May 2025,
Accepted 14th September 2025

DOI: 10.1039/d5cy00606f

rsc.li/catalysis

The development of innovative layered materials having economical and high specific surface areas could offer effective solutions for sustainable development. In this context, MXenes, known for their high surface area, tunable structures, and rich surface chemistry, combined with the light-absorbing and photocatalytic properties of QDs, result in composites with enhanced conductivity, optical activity, catalytic efficiency, and biocompatibility. The key objective of this research work is to investigate the recent advancements in Ti_3C_2 MXene modified quantum dot nanocomposites for energy conversion and environmental applications. The authors intend to guide readers through various features, including the exceptional properties, synthesis methods, and recent advancements related to MXene modified quantum dot (QD) nanocomposites. This review serves as a comprehensive resource for prospective researchers to deepen their understanding of the applications of MXene modified QDs in various fields, including water splitting, CO_2 reduction, and environmental remediation. Finally, the review addresses the on-going issues and provides insights into future guidelines for research in MXene modified QD nanocomposites, emphasizing their role in advancing sustainable photocatalytic technologies.

1. Introduction

The overconsumption of fossil fuels has obstructed sustainable development, causing an energy crisis, climate change, and social inequalities, making the transition to renewable energy and sustainable practices essential for a better future. Among the various green and renewable energy technologies being explored, semiconductor photocatalysis stands out as one of the most promising due to its capacity to harness natural sunlight and its potential for photochemical conversion. This makes it a highly viable alternative for addressing the energy and environmental challenges of the future. Harnessing clean, abundant, and renewable solar energy through photocatalytic processes such as hydrogen evolution, CO_2 reduction, and environmental remediation offers a promising strategy to meet the growing energy demand and address environmental awareness.[1–5] Key processes in photocatalysis include solar energy assimilation, generation of photoinduced charge carriers, spatial charge segregation, and heterogeneous charge transfer. Enhancing these processes can improve photocatalytic performance and optimize solar energy utilization.[2,6] As a result, extensive research focuses on developing photocatalytic materials with extended solar spectrum absorption, numerous active sites, and optimized charge segregation to maximize energy utilization.[7,8] Advancements in nanotechnology, especially in the creation of nanomaterials with diverse structures and morphologies, have significantly accelerated the development of innovative photocatalysts.[9,10] Building on the pioneering separation of graphene, two-dimensional (2D) materials have alleviated the central concern of both scientific researchers and industrial innovators over the past decade, owing to their exceptional structural, optical, and electronic characteristics, which set them apart from traditional materials.[11–13] As a result, a variety of 2D materials have continuously emerged, including oxides, layered double hydroxides, hexagonal boron nitride, black phosphorus (BP), graphite carbon nitrides (g-C_3N_4), phosphorene, and bimetallene.[14–30]

Among the various 2D materials, MXenes, a new intriguing family of two-dimensional (2D) transition metal carbides/nitrides/carbonitrides, have gained recognition as a highly promising alternative material for enhancing photocatalytic efficiency in renewable energy and environmental remediation, offering remarkable hydrophilicity, conductivity, and mechanical properties.[31] Following the pioneering work by Naguib and colleagues on the synthesis of Ti_3C_2 MXene *via* wet-chemical etching of Ti_3AlC_2 in hydrofluoric acid, followed by exfoliation, a wide variety of MXenes have since been synthesized using diverse

---

Centre for Nano Science and Nanotechnology, Siksha "O" Anusandhan (Deemed to be University), Bhubaneswar, Odisha 751030, India.
E-mail: kulamaniparida@soa.ac.in, paridakulamani@yahoo.com;
Fax: +91 674 2350642; Tel: +91 674 2351777

methods and extensively investigated in research.[32] To date, MXenes have received substantial attention due to their exceptional characteristics, including their highly metallic nature, hydrophilicity, easily tunable composition, excellent electrical conductivity, large surface area, and improved oxidative resistance.[33,34] MXenes, represented as $M_{n+1}X_nT_x$ (n = 1, 2, 3), consist of M as early transition metals (Ti, Cr, Nb, Hf, Sc, Mo, *etc.*), X representing nitrogen (N), carbon (C), or both (CN), T_x being surface groups like –F, –O and, –OH, and x refers to the number of surface groups per formula unit. $M_{n+1}X_nT_x$ sheets, bonded by van der Waals forces and/or hydrogen bonds, consist of 'n' layers of X sandwiched between 'n + 1' layers of M, such as $Ti_3C_2T_x$, $Nb_4C_3T_x$, $Zr_3C_2T_x$, Hf_2NT_x, and Ti_2CT_x. MXenes are mainly fabricated through acid etching, which selectively removes the 'A' layer (composed of group 13 or 14 elements) from their MAX or non-MAX phase precursors. In spite of bottom-up and chemical transformation methods,[35] acid etching is favored for its feasibility, control, high yield, and low cost. Moreover, the 2D MXene layers, produced by chemically exfoliating the "A" group layers from the parent MAX phase, can display a range of surface functionalizing termination groups, including –F, –O, –OH, and so on. The interaction between the element M layers and surface-induced functional terminated groups of MXenes drives the targeted functionalization of their surfaces. This has led to growing interest in the strategic blueprint and production of MXene or MXene-modified photocatalysts for a variety of photocatalytic processes, such as hydrogen evolution, CO_2 reduction, and pollutant degradation.[36–38] More than 70 MAX phases of ternary carbides and nitrides have been discovered, further broadening the MXene family, and to date, more than 30 MXenes have been experimentally synthesized, with many more predicted theoretically.[39–42] Ti_3C_2 MXene, with its layered structure, metallic conductivity, tunable terminal groups, and ease of morphological modification, is recognized for its significant advantages in photocatalytic processes, highlighting it as a leading co-catalyst to enhance photocatalytic performance. Because of its lower Fermi level compared to conventional semiconductors, metallic MXene is employed as a co-catalyst in semiconductor photocatalysts.[43] Therefore, not only Ti_3C_2 MXenes but also Ti_3C_2 MXene-modified nanocomposites have been associated with substantial research interest, with great interest in energy storage and conversion.

MXene heterostructures with 0D, 1D, and 2D nanomaterials enhance efficiency, with 0D nanomaterials being particularly valued for their simplicity, flexibility, and unique electronic properties. Quantum dots (QDs) are 0D materials with dimensions smaller than the exciton Bohr radius, exhibiting unique properties like quantum confinement, visible light absorption, a multiexciton effect under illumination, and numerous surface-active sites. These characteristics make quantum dots (QDs) highly promising for applications in catalysis, energy conversion, artificial photosynthesis, and chemical transformation. The quantum confinement principle provides QDs a strong driving force for proton reduction, enabling easy tuning of their band gaps by altering their size and extending their light absorption capabilities into the infrared spectrum. By adjusting the size and composition ratio of QDs, their photon absorption can be significantly broadened, potentially covering the entirety of the solar spectrum. Additionally, QDs have symmetrical and narrow emission spectra, which minimize interference during polychromatic excitation. Again, compared to bulk semiconductor materials, semiconductor QDs exhibit inimitable multiexciton properties, enabling the generation of multiple excitons from a single photon absorption.[44–48] The small particle size of QDs facilitates rapid charge separation and transmission due to the short distance from the solid to the surface for photoelectronic transmission. In photocatalytic reactions, the unique multi-exciton production in QDs can lead to high quantum efficiency (even exceeding 100%), an enlarged specific surface area for interaction, and improved light absorption capabilities due to a higher light absorption coefficient. Due to their highly diverse properties, quantum dots (QDs) have a comprehensive range of potential applications, including sensing, cancer treatment, catalysis, biomedical fields, optoelectronics, energy storage, and energy conversion. Additionally, integrating QDs with 2D materials in heterostructures further boosts their efficiency for an extensive range of applications.[49–52] Hence, the 0D–2D coupled interfaces have garnered significant attention due to their unique benefits, such as enhanced photocatalytic activity, improved stability, self-cleaning abilities, high efficiency in dye removal, and versatility across different applications, especially when compared to 0D–2D, 0D–1D, 1D–1D, and 1D–2D interfaces. In this context, MXene-modified QDs have sparked significant curiosity and have facilitated new opportunities for an extensive range of applications. The MXene-modified QDs have intriguing characteristics such as good biocompatibility, excellent photoluminescence, natural hydrophilicity, relative ease of functionalization, and high thermal/mechanical properties. Recently, several reviews have been published on Ti_3C_2 MXene-modified materials for various applications. Reviews on MXene-modified nanocomposites, such as MXene/LDH, MXene/TiO_2, and MXene/MOF, focus on enhancing properties like conductivity, surface area, and stability for improved performance in energy conversion and environmental applications. The hybridization of quantum dots with Ti_3C_2 MXene to form Ti_3C_2 MXene/QDs nanocomposites enhances energy conversion and environmental applications due to the synergistic properties of both components. Therefore, a review dedicated explicitly to Ti_3C_2 MXene-modified QDs nanocomposites for photocatalytic applications is highly anticipated, though it has not yet been conducted. This work seeks to offer a comprehensive and detailed summary of the recent ongoing developments in Ti_3C_2 MXene/QDs nanocomposites in the field of energy conversion and environmental applications.

This review provides an overview of recent advancements in "MXene-modified quantum dots", focusing on their innovative applications and enhanced properties across various fields. It explores the structural properties and synthesis methods of Ti_3C_2 MXene-modified quantum dots and their electrochemical, optical, morphological, and structural features in nanocomposites. The review also investigates how combining the properties of Ti_3C_2 MXene and quantum dots in nanocomposites can significantly boost performance in energy conversion and environmental remediation. Although our group has published reviews on QDs and MXenes separately, a comprehensive review on the photocatalytic applications of MXene-modified QDs is still lacking.[28–30] In order to have a unified vision of the field, this review attempts first to summarize how the performance of Ti_3C_2 MXene-modified QD nanocomposites can expand their potential applications, and outlines future improvements in energy storage, conversion, and other photocatalytic applications.

2. Structural properties of MXenes and quantum dots

MXenes exhibit distinct properties, including a high Young's modulus, electrical conductivities, superior thermal stability, variable band gaps, hydrophilic textures, and high metallic conductivities, distinguishing them from other 2D materials such as graphene oxide (GO).[53] Moreover, surface functional groups and morphological alterations enable the tuning of MXene properties and applications.[54,55] However, bare MXenes are metallic and inactive in photocatalysis. Nevertheless, surface functionalization can transform them into semiconductors by introducing new energy levels below the Fermi level and shifting the Fermi level to a lower energy. Although MXenes have a nearly zero bandgap, it can be adjusted to some degree through surface adsorption groups. DFT calculations by Tang *et al.* and his group indicated that bare Ti_3C_2 has a larger electron density near the Fermi level, showing metallic characteristics,[56] but when –OH and –F groups are adsorbed onto the surface, the energy band structure of $Ti_3C_2T_x$ MXene shifts, resulting in a bandgap of 0.03–0.04 eV for $Ti_3C_2F_2$ and 0.05–0.07 eV for $Ti_3C_2(OH)_2$. Similarly, Naguib *et al.* and their coworkers reported band gaps of 0.05 eV for the –F terminated $Ti_3C_2T_x$ and 0.1 eV for the –OH terminated version.[57] However, the continuous electronic states that cross the Fermi level for –O and –F terminated $Ti_3C_2T_x$ show excellent conductivity. As a result, $Ti_3C_2T_x$ maintains its excellent electrical conductivity even after being modified with various functional groups, demonstrating its remarkable ability to transport charge carriers.[58] Therefore, metallic MXenes typically exhibit a work function ranging between 1.8 and 8 eV. In contrast, MXenes having semiconducting properties exhibit bandgaps between 0.05 and 2.87 eV, which can be controlled through compositional adjustments. For example, theoretical studies using PBE functional computations have predicted bandgaps for various functionalized MXenes as follows: Sc_2CF_2 (1.03 eV), Sc_2CO_2 (1.80 eV), Zr_2CO_2 (0.88 eV), Ti_2CO_2 (0.24 eV), Hf_2CO_2 (1.0 eV), and $Sc_2C(OH)_2$ (0.45 eV). On the other hand, some MXenes, such as Cr_2C and Cr_2N, exhibit magnetic properties, while others, like Ti_3C_2, Ti_5C_4, Ti_4C_3, Ta_3C_2, Ti_4N_3, V_4C_3, V_3C_2, Nb_4C_4, Nb_4C_3, and Ta_4C_3, retain their metallic characteristics despite different surface functional groups. The work functions of MXenes are influenced by charge transport across the interface between the functional groups and the MXene surface, as well as by shifts in the net surface dipole moments resulting from surface relaxation. For instance, MXenes with –OH terminations exhibit work functions between 1.6 and 2.8 eV, while those with –O (oxygen) terminations exhibit higher work functions between 5.75 and 6.25 eV. Hence, the work function of MXenes, which influences electron trapping, can be adjusted through careful design. Similar metallic characteristics were observed for $Ti_3C_2T_x$ MXene, emphasizing that surface termination can significantly modify the optoelectronic properties of MXenes. The fluctuations in bandgap energy resulting from different surface terminations follow the order: $–O_2 > –F_2 > –(OH)_2$. Again, a theoretical study showed that functional groups can cause MXenes to shift from metallic to semiconducting behavior, as seen in $Sc_2C(OH)_2$, Sc_2CF_2, Ti_2CO_2, Zr_2CO_2, Sc_2CO_2, and Hf_2CO_2. This transition happens due to variations in electronegativity between the transition metals and the X atom, along with the attached functionalization. However, in thicker MXenes with multiple transition metals, surface functionalization does not alter their metallic properties, as seen in $Ti_3C_2T_x$, which remains metallic and does not exhibit semiconducting properties. Again, tailoring these surface terminations can modify the catalytic properties and carrier density of $Ti_3C_2T_x$ MXene. Different terminations in MXenes can alter their metal work functions, as well as their structural, electrical, and optoelectronic properties. Further, the functional groups on MXene nanosheets are distributed randomly across the surface, rather than being confined to specific areas. The HF concentration influences the chemical composition of these functional groups; lower HF concentrations result in a higher –O/–F ratio, while higher concentrations favor a higher –F/–O ratio. For example, etching the Ti_3AlC_2 MAX phase with 10% HF or LiF/HCl produces $Ti_3C_2T_x$ MXenes with a predominance of –O over –F, while using 50% HF leads to MXenes with more –F groups than –O.[59,60] Therefore, this functionalization has a noteworthy effect on the chemical and electrical properties of MXenes.[61] Even though controlling surface terminations is challenging, experimental studies have shown that different etching chemicals can influence the types of terminations. For instance, –OH terminations can enhance photocatalytic activity by promoting the formation of active TiO_2, though rapid oxidation could be a drawback. Further, advances in $Ti_3C_2T_x$ MXene preparation techniques, including delamination and intercalating agents, underscore its versatility. Therefore, the interaction between termination groups and the structure of $Ti_3C_2T_x$ MXene is crucial for optimizing its catalytic performance. The type of termination group in MXenes is influenced by several factors: the technique used for the etching process, the number of MXene layers, and the properties of the M and X elements. Quantitative nuclear magnetic resonance spectroscopy analysis revealed that $Ti_3C_2T_x$ multilayers produced through HF etching contained four times more fluorine than those etched with HCl/LiF (ref. 62) and had significantly lower OH terminating groups. Further, Voigt *et al.* and coworkers[63] illustrated that multiple layers of $Ti_3C_2T_x$ exhibited increased interlayer spacing when etched with HF in combination with another type of acid, like HCl and HBr, concluding that anions adsorbed along the edges of the nanosheets contributed to the larger spacing. Halim *et al.*[64] conducted X-ray photoelectron spectroscopy on various multilayer MXenes and found that most of the termination groups are fluorine, although this changes to oxygen over time. For titanium-based MXenes, altering "*n*" from 1 to 2 or changing "X" from C to N only affects the ratio of hydroxyl to oxygen terminations. Specifically, increasing "*n*" from 1 to 2 enhances the O to OH ratio, while decreasing the carbon content in favor of nitrogen reduces this ratio. Additionally, the MXene termination can be modified during the exfoliation process, as demonstrated by the use of tetrabutylammonium hydroxide (TBAOH) to delaminate HF-etched MXenes,[65] which enhanced oxygen terminations at the expense of fluorine, indicating that the latter is thermodynamically unstable. The chemical properties of MXenes can also be analyzed through post-synthesis methods. *In situ* heating studies of $Ti_3C_2T_x$ thin films showed that fluorine terminations began to desorb at 500 °C and were completely removed by 700 °C.[66] Additionally, the fluorine as a terminating group in MXene multilayers may react with alkali hydroxides, replacing them with oxygen or hydroxyl terminations.[67] The effectiveness of MXenes in photocatalysis often relies on their electrical conductivity and work function, influencing hydrogen generation and other photocatalytic activities. Functionalization and intercalation can modify electronic properties, and different types of termination groups and intercalating agents impact these properties. Despite its unique structural and morphological flexibility, Ti_3C_2 MXene suffers from low oxidation stability, where titanium atoms oxidize to form titanium dioxide, while the carbon atoms remain unchanged.[68] This formation of TiO_2 can be advantageous in some technological applications, like photocatalysis, because the active material generated through oxidation can enhance the photocatalytic properties of Ti_3C_2 MXene, improving solar energy conversion through synergistic effects between Ti_3C_2 and its oxide form.[69,70] Further, Ti_3C_2 MXene is thermally stable, with a decomposition temperature ranging between 2000–3000 °C,[71] with the transition metal choice influencing its stability and being crucial for optimizing properties through heat treatment for specific applications. Hence, customizing these properties is essential for enhancing MXenes' performance in diverse energy evolution and environmental applications.

Moreover, quantum dots (QDs) are semiconductor nanosized materials with exceptional optical and electronic properties because of their small size and quantum confinement. As QD size reduces, their band-gap increases, and the electron and hole form an exciton with lower energy. When the QD radius approaches the exciton Bohr radius (rB), electron–hole confinement leads to a blue shift in the band-gap and luminescence. Smaller QDs have higher exciton and biexciton binding energies compared to bulk materials. The exciton Bohr radius depends on the material's dielectric constant and the effective masses of the electron and hole. Excitation of the material by photons, electric fields, or electrons promotes the electron and hole to an excited state, where they can recombine, releasing excess energy as either radiative or nonradiative energy. Quantum dots (QDs) are commonly classified according to their chemical composition, which plays a vital role in shaping their structural characteristics, chemical durability, and optical performance. They are basically classified under two categories: carbon based QDs such as carbon, grapheme, MXene and noncarbon QDs such as chalcogenide, oxides, prosperous, perovskite, silicon, and noble metal. Among the various types, semiconductor quantum dots are the most thoroughly researched. These are generally composed of elements from groups II–VI, III–V, or IV–VI of the periodic table. These materials include cadmium selenide (CdSe), cadmium telluride (CdTe), indium phosphide (InP), and lead sulfide (PbS). Semiconductor quantum dots are unique due to quantum confinement, where their tiny size (2–10 nm) influences electron behavior, resulting in size-dependent photoluminescence, enabling their emission color to be adjusted from ultraviolet to infrared where smaller dots emit blue light, while larger ones emit red. Cadmium-based quantum dots like CdSe and CdTe are prized for their brightness, narrow emission, and high efficiency, making them useful in biolabeling, QLEDs, and lasers. However, their toxicity limits use, driving interest in safer alternatives like indium phosphide (InP) QDs. InP QDs offer similar performance without heavy-metal risks and are increasingly used in commercial products like next-gen QLED TVs, providing vibrant, high-quality colors while meeting safety regulations. The composition of semiconductor quantum dots shapes their optical behavior, safety for biological and environmental use, and commercial success. Efforts continue to refine these materials for better performance, lower toxicity, and greater long-term reliability. Carbon quantum dots (CQDs) are made from carbon-rich materials like graphite or organic compounds. They are biocompatible, water-soluble, and environmentally friendly, with strong photoluminescence and chemical stability. These properties make them ideal for bioimaging, drug delivery, and environmental sensing. Graphene quantum dots (GQDs), closely related to CQDs, are nanoscale fragments of graphene or graphene oxide. They offer excellent electrical conductivity, mechanical strength, and tunable emission, making them suitable for biosensing, photovoltaics, and flexible electronics. Perovskite quantum dots, such as those made from cesium lead bromide ($CsPbBr_3$) or methylammonium lead iodide ($MAPbI_3$), represent a newer class known for their high light-emission efficiency, narrow emission spectra, and color purity. These properties make them attractive for LEDs, lasers, and solar cells. However, their instability and lead content pose challenges for large-scale and long-term use. Silicon quantum dots (SiQDs) are composed of elemental silicon and are known for their low toxicity and compatibility with existing semiconductor technologies. While their light emission is not as efficient as that of traditional QDs, they are valued for their biocompatibility, making them suitable for medical imaging and biosensing. Lastly, doped quantum dots are formed by introducing dopant atoms (such as manganese, copper, or rare-earth elements) into the QD structure. These dopants add new optical, magnetic, or electronic functionalities, enabling advanced applications in spintronics, MRI imaging, and luminescent tagging. In conclusion, the composition of quantum dots significantly influences their optical properties, toxicity, stability, and application potential. While some, like Cd-based QDs, offer high performance but raise toxicity concerns, others like carbon and silicon QDs provide safer alternatives with slightly lower efficiency.

3. Preparation methods of MXene-modified QDs photocatalysts

MXenes play multiple key roles in photocatalytic nanocomposites, enhancing their efficiency for many applications such as water splitting, pollutant degradation, and carbon dioxide reduction. Because of their lower Fermi level and superior electronic conductivity, MXenes are effective cocatalysts that improve the separation of charge carriers produced by photon absorption. Again, as a supporter, they stabilize and disperse other photocatalysts, improving stability and maximizing light absorption. Further, MXenes enhance charge carrier migration, increase active sites, and can be modified to optimize surface properties for specific reactions. Their high conductivity, large surface area, and tunable properties make MXene-modified composites highly effective in various photocatalytic processes. Therefore, multiple heterostructures incorporating two-dimensional MXenes have been developed for photocatalysis and photocatalytic applications. Moreover, MXene-modified quantum dot nanocomposites combine the unique properties of quantum dots with the 2D structure of MXene, enhancing the photocatalytic performance, charge separation, and stability, while enabling tunable properties and increased surface area for applications in energy storage and pollutant degradation. Based on different synthesis processes followed, MXene-modified heterostructures can be categorized into:

1. Mechanical mixing/self-assembly.
2. *In situ* decoration.
3. *In situ* oxidation.

3.1. Mechanical mixing or self-assembly

Mechanical mixing or self-assembly is the easiest method for preparing heterojunction photocatalysts for different practical applications. This can be achieved by stirring two nanocomposite components in a liquid phase or grinding powders together to prepare the sample. Self-assembly of component molecules at the nanoscale is a process observed in nature, where soft materials naturally form structures such as cell membranes, biopolymer fibers, and viruses. Recently, scientists and engineers have harnessed this concept in the laboratory to create nanostructured materials through a bottom-up approach known as self-assembly. This method involves the spontaneous organization of nanoscale materials into well-defined superstructures, which can be used for various applications. Self-assembly also refers to the process where isolated samples spontaneously organize into controlled structures to minimize the system's free energy. Among the multiple methods, electrostatic self-assembly is particularly popular due to its simplicity and effectiveness in synthesizing hetero composites. This gentle process not only ensures a narrow size distribution but also improves the control over the morphology of the final product.

MXenes, being negatively charged due to their surface functional groups, easily self-assemble with positively charged photocatalysts. The mechanical mixing can be achieved through sonication, stirring, or grinding. Self-assembly typically occurs due to the inherent chemical and physical interactions between the MXene layers and other materials, leading to the formation of well-defined heterojunctions. This method is straightforward, operates under mild conditions, effectively prevents oxidation, and preserves the surface functional groups. 2D MXene-based heterojunction photocatalysts are popular due to their enlarged surface area and unsaturated sites. Shi-Cheng Zhu *et al.* mixed colloidal $Ti_3C_2T_x$ MXene with AET-capped CdSe QDs in different weight proportions (0.5, 1, 2, and 4 wt%) and stirred the mixture for 60 minutes, followed by centrifugation, washing, and drying to obtain CdSe QDs–MXene nanocomposites.[72] In both processes, the properties of MXenes are preserved by avoiding high temperatures and using additional solvents or surfactants. Further, oxidation and surface termination groups remain unaffected during these synthesis processes. As a result, these methods are found to be the simplest and enable synthesis under the optimal mild conditions.

3.2. *In situ* decoration

Unlike composites made through mechanical mixing, *in situ* decoration methods involve preparing a different material directly on the surface of MXenes. This leads to a chemical bond between the *in situ* synthesized substrate material and MXenes, which leads to a significant advantage in many applications. However, the range of viable synthetic conditions for *in situ* decoration is limited, due to the tendency of MXenes to oxidize in solution, particularly at high temperatures. Thus, it is crucial to use mild conditions to safeguard MXenes from oxidation, particularly when working with mono- or few-layered MXenes. MXenes have been *in situ* decorated with semiconductors like TiO_2, C_3N_4, CdS, perovskites, *etc.* The synthesis process for MXene-modified nanocomposites typically involves either doping photocatalysts with MXenes or using MXenes as a support material for the *in situ* decoration of semiconductor photocatalysts. The chemical reactions involved during the formation of the photocatalysts enhance the interfacial area, thereby increasing the potential for the transport of light-induced electrons. However, a significant drawback of this process is the oxidation of MXenes during the photocatalytic synthesis process. Despite the precise characterization being challenging, the conditions employed during the photocatalyst formation can be overly harsh, leading to structural degradation of MXenes, particularly for single-layered variants, which are less stable against oxidation.

3.3. *In situ* oxidation

In addition to mechanical mixing and *in situ* decoration, the *in situ* oxidation method has also been investigated for synthesizing MXene-modified heterostructures. Common routes for oxidizing MXenes to form metallic oxides include chemical oxidation, hydrothermal treatment, calcination, and high-energy ball milling. The hydrothermal method involves the production of substances through chemical reactions in a sealed, heated solution under high-pressure and high-temperature conditions, surpassing ambient levels. In 19th-century earth science, the term "hydrothermal" refers to systems characterized by high temperature and water pressure. This method offers several advantages, including relatively moderate operating conditions, a one-step synthesis process, environmental sustainability, and efficient diffusion within the solution. Additionally, hydrothermal synthesis is cost-effective in terms of energy, equipment, and material precursors when compared to other solution-based synthesis methods.

Typically conducted in a sealed autoclave at elevated temperatures and pressures, this method produces hetero composites with enlarged crystallinity and narrow size distribution. Consequently, hydrothermal synthesis facilitates the production of MXene-supported QD photocatalysts with consistent performance, such as the TiO_2QDs/Ti_3C_2 hybrid nanocomposite. Weiming Li and his group synthesized the TiO_2 QDs/Ti_3C_2 MXene composite by mixing TiO_2 QDs and Ti_3C_2 MXene nanosheets in water, stirring, and ultrasonically treating.[73] After heating in an autoclave, the mixture was centrifuged, washed, and dried to obtain composites. Different composite variations were achieved by adjusting the Ti_3C_2 MXene concentration. The solvothermal technique closely resembles the hydrothermal process, but instead of using water, it employs organic solvents in the synthesis. These methods are crucial for synthesizing nanocomposites with high crystalline quality. The solvothermal approach is particularly notable for its effectiveness in producing MXene-supported semiconductor photocatalysts with various structural morphologies. In this process, the autoclave is filled with organic solutions and subjected to high-temperature and high-pressure conditions to promote the reaction. The oxidation of MXenes differs from other processes due to the residual carbon (primarily in an amorphous form) remaining after oxidation, which leads to the M element being transformed into a metal oxide deposited on the carbon layer. Consequently, the resulting nanocomposite consists of metal oxide/MXenes/C, with both MXenes and carbon acting as co-catalysts in the photocatalytic process. However, in this method, the ratio of the photocatalyst to MXenes is carefully controlled within a defined range, without introducing any precursor. Moreover, this method is limited because only a specific range of semiconductors, influenced by the metal element, can be the photocatalyst.

4. Synthesis, design, and morphological characterization of MXene-modified QD photocatalysts

Various synthesis techniques of QDs incorporating MXene-based heterostructures are discussed in this section. Moreover, the characterization technique plays a crucial role in exploring the properties and structure of the synthesized material and whether the method was successful. In this section various quantum dots (QDs) like phosphorus, oxide, selenide, halide perovskites, platinum, sulfur, and carbon, were combined with MXene to synthesize nanocomposites to enhance their electronic and optical properties, opening up new possibilities in photocatalytic energy and environmental applications, making these heterostructures a key area of research in materials science (Scheme 1). Among different characterization techniques, the X-ray diffraction (XRD) technique offers detailed insights into the crystal structure, lattice parameters, phase, and crystalline grain size. X-ray Absorption Spectroscopy (XAS), which encompasses both Extended X-ray Absorption Fine Structure (EXAFS) and X-ray Absorption Near Edge Structure (XANES, also known as NEXAFS), is an element-specific technique that analyzes the X-ray absorption coefficient to provide information on the chemical state of species, interatomic distances, and structural disorder (*e.g.*, Debye–Waller factors). X-ray photoelectron spectroscopy (XPS) is a powerful quantitative technique employed for elucidating the electronic structure, elemental composition, oxidation states, and ligand binding (surface-sensitive). An XPS analysis was conducted to

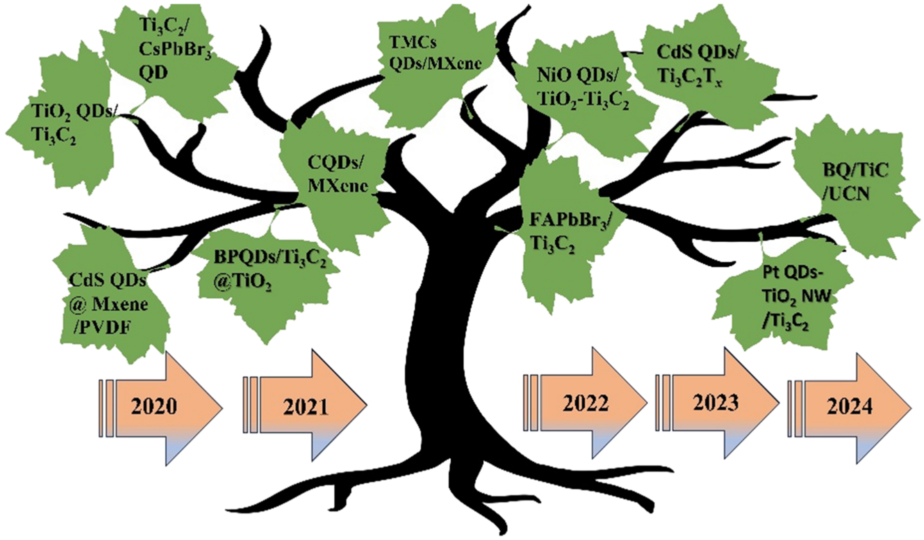

Scheme 1 Schematic illustration for a timeline of recent progress of various MXene-modified quantum dots for photocatalytic energy and environmental applications.

investigate the surface chemical properties of the samples. In nanomaterial design, Fourier-transformed infrared spectroscopy (FTIR) analysis gives evidence of molecular vibration with data associated with the strength and characteristics of the bonds and particular functional groups, thus helpful in determining surface composition and ligand binding. Another quantitative analytical technique used for structural determination of nanosized materials is nuclear magnetic resonance (NMR) spectroscopy. Essentially, the concentration and organization of ligands, the configuration of the electronic core, the elemental composition, the effect of ligands on the nanoparticle's geometry, and the particle's dimensions are the basic findings of the NMR technique. Again, the Brunauer–Emmett–Teller (BET) technique is used to measure a gas's physical adsorption on the surface of a solid. Similarly, thermal gravimetric analysis (TGA) provides detailed evidence regarding the composition and mass of the stabilizers. To understand the optical properties of photocatalysts with additional information like size, agglomeration state, concentration, and hints on nanoparticle shape, UV-vis spectroscopy (UV-vis) is used. Similarly, photoluminescence (PL) spectroscopy is another frequently used technique investigating the emission phenomenon and its optical properties concerning structural characteristics such as composition, size, and defects. A higher PL peak indicates lower efficiency in the migration and separation of charge carriers. From morphological aspects, Transmission Electron Microscopy (TEM) is an efficient technique to measure nanoparticle size, aggregation state, monodispersity, detect, and shape, and to localize/quantify nanoparticles in matrices, along with studying growth kinetics. Similarly, high-resolution transmission electron microscopy (HRTEM) gives all the information from conventional TEM, along with the crystalline structure of single particles, and differentiates between amorphous, monocrystalline, and polycrystalline NPs. HRTEM measurements were conducted to further elucidate the samples' internal structure. Scanning electron microscopy analysis (SEM) is an electron microscopy technique that can provide high-resolution images of a sample surface, allowing visualization of details about less than 1 to 5 nm in size by scanning it with a high-energy electron beam in a raster scan pattern. Energy dispersive X-ray (EDX) is an analytical technique employed for elemental characterization of the sample, whereas atomic force microscopy (AFM) measures the thickness of the nanosheet materials. To further elucidate the synthesized samples' photoinduced charge carrier transfer ability and electronic conductivity, transient photocurrent response curves and electrochemical impedance spectra (EIS) were analyzed.

4.1. MXene-modified phosphorus-based quantum dots

Phosphorus quantum dots are ultrasmall nanoscale semiconductor materials that exhibit distinct optical and electronic characteristics due to the quantum confinement and edge effect.[74] Due to its excellent charge carrier mobility, a different band gap, and high on–off current ratios,[75] black phosphorus (BP) has started gaining attention with its puckered structures along the armchair direction and its bilayer configuration along the zigzag direction.[76] Zero-dimensional black phosphorus quantum dots (BPQDs), derived from bulk black phosphorus (BP) through liquid exfoliation, possess unique photophysical and electrochemical properties, providing excellent stability, high photoluminescence quantum yields, and intense light absorption, making them ideal for applications in lithium storage, fluorescent probes, and organic photovoltaics (OPVs). Their adjustable bandgaps, which can approach nearly 3 eV, position them as promising candidates for visible-light-responsive photocatalysts. Additionally, the smaller size of quantum dots facilitates easier formation of contact interfaces compared to larger materials, which improves the transfer of light-induced electrons and improves absorption of visible light. Following the solvothermal method, which synthesizes nanomaterials by using a solvent at elevated temperature and pressure in a sealed vessel near or above the boiling point of the reaction medium, Yao *et al.* employed this method to synthesize the hybrid nanomaterial BPQDs/Ti_3C_2@TiO_2 (BTTC).[77] Again, during the synthesis, the precipitation samples of Ti_3C_2@TiO_2 are accumulated and labeled as TC (without the hydrothermal treatment) and TTC-*x* (*x* represents the temperature in °C: 100, 120, 140, and 160). As depicted in Fig. 1(a), the novel BPQDs/Ti_3C_2@TiO_2 composites are created through the *in situ* growth of TiO_2 nanoparticles on the surface of Ti_3C_2, followed by the introduction of BPQDs to form a heterojunction nanostructure. Moreover, the surface of the BTTC-120 heterostructure becomes rough due to TiO_2 NPs' formation, indicating their growth on Ti_3C_2 during the hydrothermal process, as seen in FESEM images. Similarly, HRTEM images, Fig. 1(b–d), reveal the production of a heterojunction between BPQDs and TiO_2 nanoparticles on Ti_3C_2. Further, Fig. 1(e) demonstrates that the BTTC-*x* heterostructure enhanced the light absorption compared to the BTC sample, representing improved optical performance due to hydrothermal oxidation. Similarly, Fig. 1(f) shows that BTTC-120 has the largest specific surface area (15.29 m^2 g^{-1}) due to TiO_2 NPs on Ti_3C_2 nanosheets, enhancing reactant adsorption and migration, compared to BTC (3.15 m^2 g^{-1}) and TTC-120 (10.55 m^2 g^{-1}).[78] Again, from Fig. 1(g), BTTC-120 has a higher photocurrent than BTC and TTC-120 samples, showing improved separation of photo-generated carriers due to BPQD loading and hydrothermal oxidation.

In addition, Song and his research group designed the ternary BQ/TiC/UCN heterojunction using grinding and sonication, which improves interfacial interaction and visible-light capture capacity by enhancing solution mixing and solid dissolution (Fig. 2(a)).[79] Conventional bulk g-C_3N_4 faces several limitations, including low surface area, poor adsorption capacity, and significant charge carrier recombination, all of which restrict its practical implementation. Nevertheless, merely creating an ultrathin g-C_3N_4 nanosheet (UCN) is insufficient to significantly improve the transport of light-induced exciton pairs and the absorption of visible light. Again, integrating UCN with other materials to construct a semiconductor heterojunction offers a promising strategy to improve its photocatalytic performance. Further, when BP nanosheets are reduced to

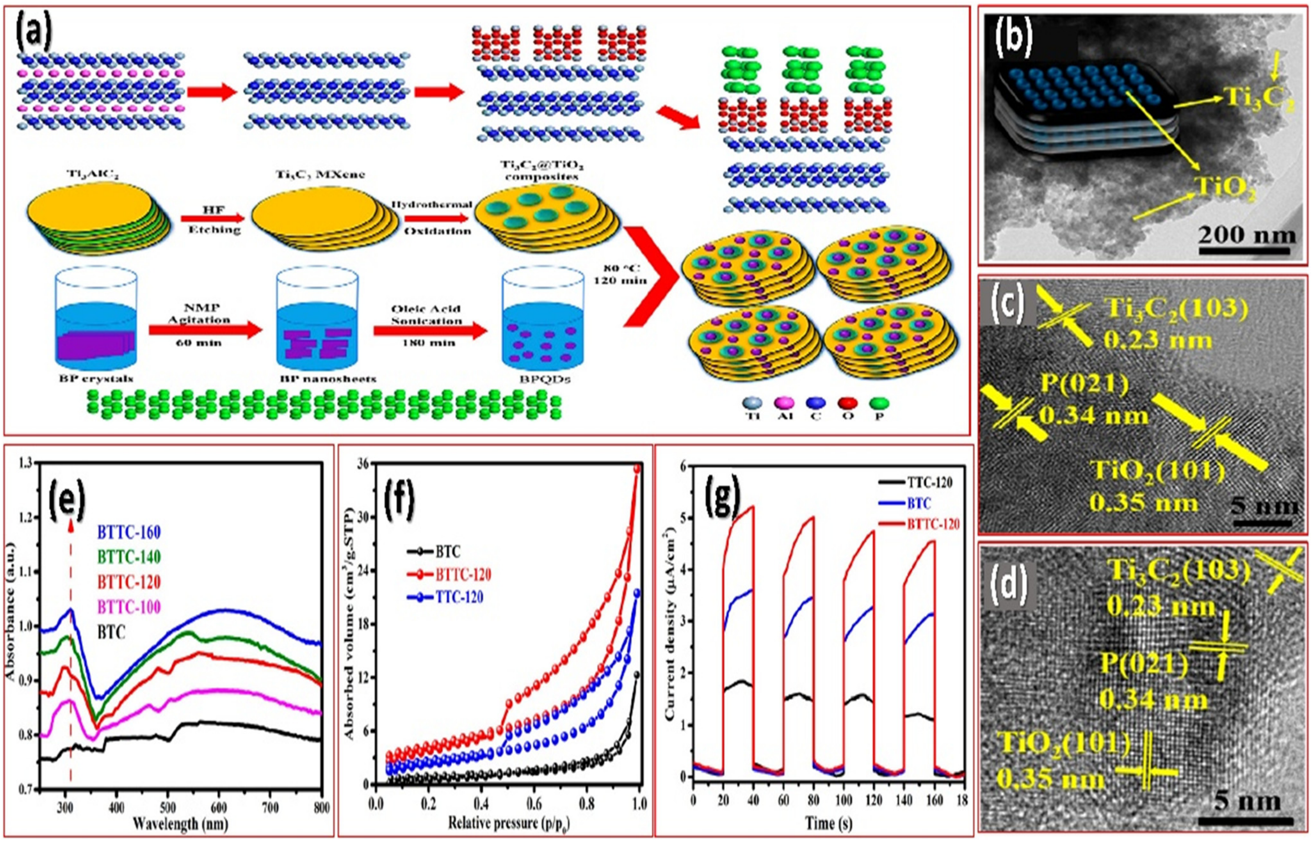

Fig. 1 (a) Schematic illustration of the preparation of BPQDs/Ti_3C_2@TiO_2 composites, (b–d) HRTEM images of the BTTC-120 sample, (e) UV-vis diffuse reflectance spectra (DRS) of as-synthesized BTC and BTTC-*x* (*x* = 100, 120, 140, and 160 °C, respectively), (f) N_2 adsorption–desorption isotherms of the as-prepared BTC, TTC-120, and BTTC-120 powders, and (g) photocurrent response. Reproduced from ref. 77 with permission from MDPI, copyright 2020.

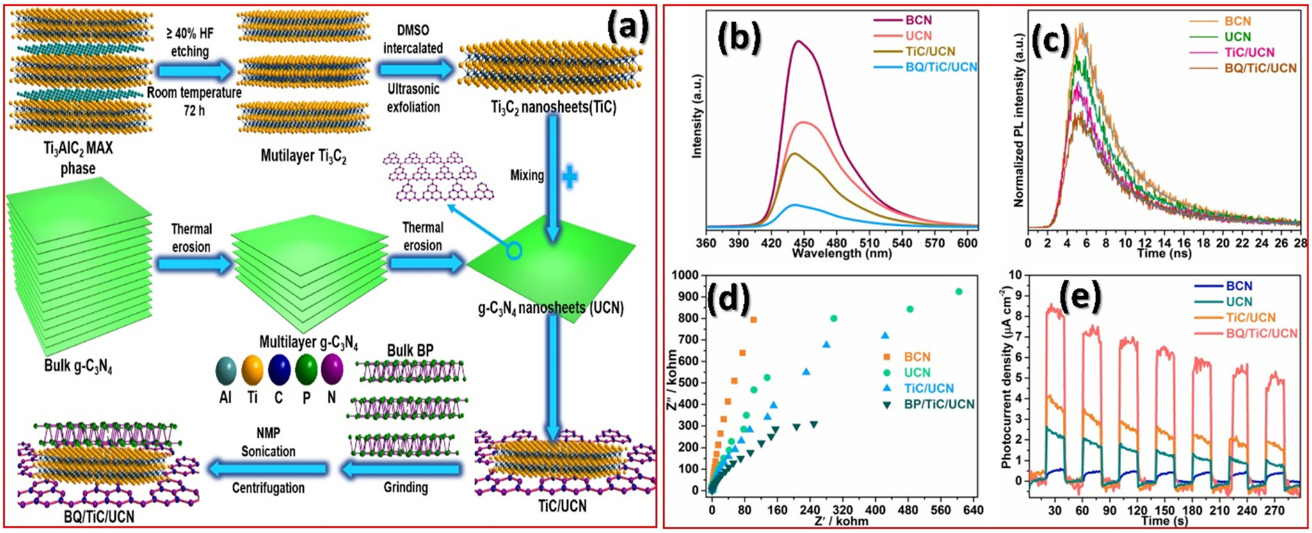

Fig. 2 (a) Illustration of the synthetic process of the optimal BQ/TiC/UCN composite, (b) steady-state photoluminescence (PL) spectra of BCN, UCN, TiC/UCN and BQ/TiC/UCN samples, (c) time-resolved PL decay profiles for BCN, UCN, TiC/UCN and BQ/TiC/UCN samples, (d) electrochemical impedance spectra (EIS) of BCN, UCN, TiC/UCN and BQ/TiC/UCN samples, and (e) transient photocurrent responses of BCN, UCN, TiC/UCN and BQ/TiC/UCN samples. Reproduced from ref. 79 with permission from Elsevier, copyright 2020.

less than 20 nm in diameter, they become BP quantum dots (BQ), which offer enhanced edge effects, high absorption coefficients, quantum confinement, and ease of hybridization with other materials compared to their bulk counterparts. Moreover, the study examines the photoluminescence (PL) and charge transfer properties of various photocatalyst samples: BCN, UCN, TiC/UCN, and BQ/TiC/UCN showing that BQ/TiC/UCN exhibits significantly reduced PL intensity and shorter charge carrier lifetimes compared to the other samples, showing more efficient charge separation and reduced recombination as depicted in Fig. 2(b). Similarly, time-resolved PL tests Fig. 2(c) demonstrate that the lifetimes of BQ/TiC/UCN (τ_1 = 1.81 ns, τ_2 = 5.32 ns) are shorter than BCN, UCN, and TiC/UCN, with average lifetimes of 5.60 ns for BQ/TiC/UCN, compared to 13.95 ns for BCN. The shorter decay time of BQ/TiC/UCN indicates enhanced charge migration and reduced recombination of photogenerated exciton pairs, facilitated by the interfacial interaction between BQ and UCN through ultrathin TiC. Again, from Fig. 2(d), electrochemical impedance spectroscopy (EIS) and transient photocurrent measurement tests further confirm that BQ/TiC/UCN has superior charge transfer efficiency and photocurrent response. Additionally, the transient photocurrent response, Fig. 2(e), was used to assess the improved charge transfer efficiency.[80]

4.2. MXene-modified oxide-based quantum dots

Metal oxide quantum dots (MOQD) are nanoscale semiconductors that exhibit quantum confinement, resulting in unique optical, electronic, and catalytic properties. Their energy band structure suggests that they can be a good heterostructure due to their interaction with light, charge carrier generation, and transfer. In this regard, Li and his group designed ultra-small TiO$_2$ QDs coupled with large-sized Ti$_3$C$_2$ MXene nanosheets and investigated their photocatalytic properties.[73] Furthermore, to confirm the successful synthesis of ultra-small TiO$_2$ quantum dots (QDs), Fig. 3(a) presents a low-magnification TEM image, showing evenly distributed black dots smaller than 5 nm on the carbon film. Fig. 3(b and c) presents the height profile of delaminated MXene, measured by AFM, indicating a thickness of approximately 3.8 nm, confirming the presence of ultra-thin MXene nanosheets. The high-magnification TEM image reveals clear lattice fringes of the TiO$_2$ QDs, corresponding to the (101) lattice plane.[81] Therefore, it is evident that ultra-small photocatalysts have been effectively anchored onto the surface of large-sized cocatalysts.

4.3. MXene-modified selenide-based quantum dots

Chalcogen-based quantum dots, such as transition metal chalcogenides (TMCs: CdSe, CdTe CdS,), are highly efficient for several reasons such as (1) strong light absorption in the visible to near-infrared regions; (2) a large specific surface area combined with short charge transfer distances; and (3) a tunable bandgap that enables the emission of multiple electrons from the valence band (VB) to the conduction band (CB) per absorbed photon.[82,83] Considering the efficiency of 0D TMCs QDs, Shi-Cheng Zhu and coworkers designed a 0D/2D CdSe QDs/MXene nanocomposite by a ligand-initiated electrostatic self-assembly strategy, Fig. 4(a), wherein positively charged CdSe QDs were anchored onto the negatively charged ultrathin Ti$_3$C$_2$T$_x$ nanosheets (NSs)' framework, facilitating the anisotropic unidirectional electron transport from CdSe QDs to MXene NSs.[72] The high conductivity of MXene facilitates the formation of Schottky junctions with TMCs QDs,[84–86] promoting efficient electron transfer. After CdSe QDs are added, the MXene surface becomes rough due to the uniform deposition of CdSe QDs,

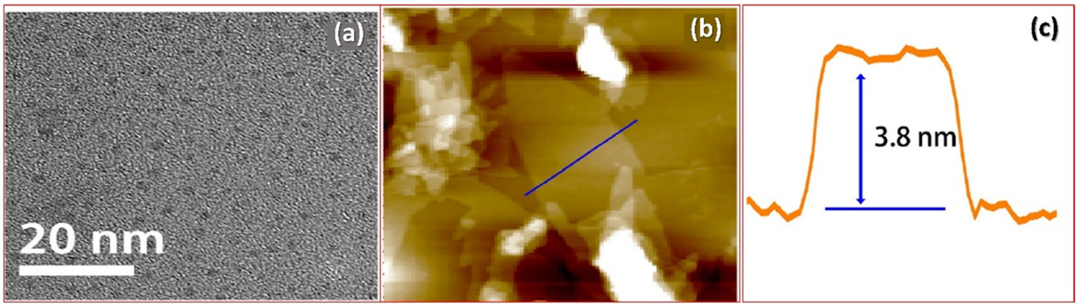

Fig. 3 (a) TEM image of TiO_2 QDs, (b) height profile characterized by AFM, and (c) the corresponding height distribution. Reproduced from ref. 73 with permission from Elsevier, copyright 2021.

forming a 0D–2D heterostructure. TEM images show that CdSe QDs are spatially dispersed and self-assembled on MXene with strong interfacial contact, Fig. 4(b). Again, Fig. 4(c and d) displays the lattice fringes of CdSe QDs and MXene having spacings of 0.35 nm and 0.26 nm, corresponding to the (111) plane of cubic-phase CdSe and the (110) plane of $Ti_3C_2T_x$ MXene, respectively. In this setup, CdSe Quantum dots are evenly dispersed on the surface of the $Ti_3C_2T_x$ MXene nanosheets, ensuring strong interfacial adhesion and enabling stable, robust performance in photoreduction catalysis.

4.4. MXene-modified inorganic halide perovskite-based quantum dots

Metal halide perovskites, such as $CsPbBr_3$, $CH_3NH_3PbI_3$, $Cs_2AgBiBr_6$, *etc.*, offer significant advantages such as a wide adsorption range, high photoluminescence efficiency, large charge carrier motility, and long-hole diffusion length.[87–90] To increase the catalytic sites and suppress the charge recombination of halide perovskite, it is coupled with a low-dimensional material such as 2D MXene due to its abundant active sites, large specific surface area, layer-dependent electronic structure, and intense interfacial contact. Moreover, Zhang and his research group synthesize a heterostructure, $Ti_3C_2/CsPbBr_3$ quantum dot ($Ti_3C_2/CsPbBr_3$ QD) through a self-assembly method.[91] The improved photocatalytic efficiency of this composite can be credited to the superior light absorption and the unique 0D/2D structure of the $Ti_3C_2/CsPbBr_3$ quantum dot composites. Moreover, the UPS spectra of $CsPbBr_3$ QDs and Ti_3C_2 in Fig. 5(a–e) provide key electronic properties such as: $CsPbBr_3$ QDs have a Fermi level depth of 4.35 eV, valence band maximum (VBM) of 5.86 eV, and a band gap of 2.41 eV, and Ti_3C_2 has a Fermi level depth of 4.19 eV, a VBM of 4.77 eV, a band gap of 1.77 eV, respectively. Therefore, this work provides

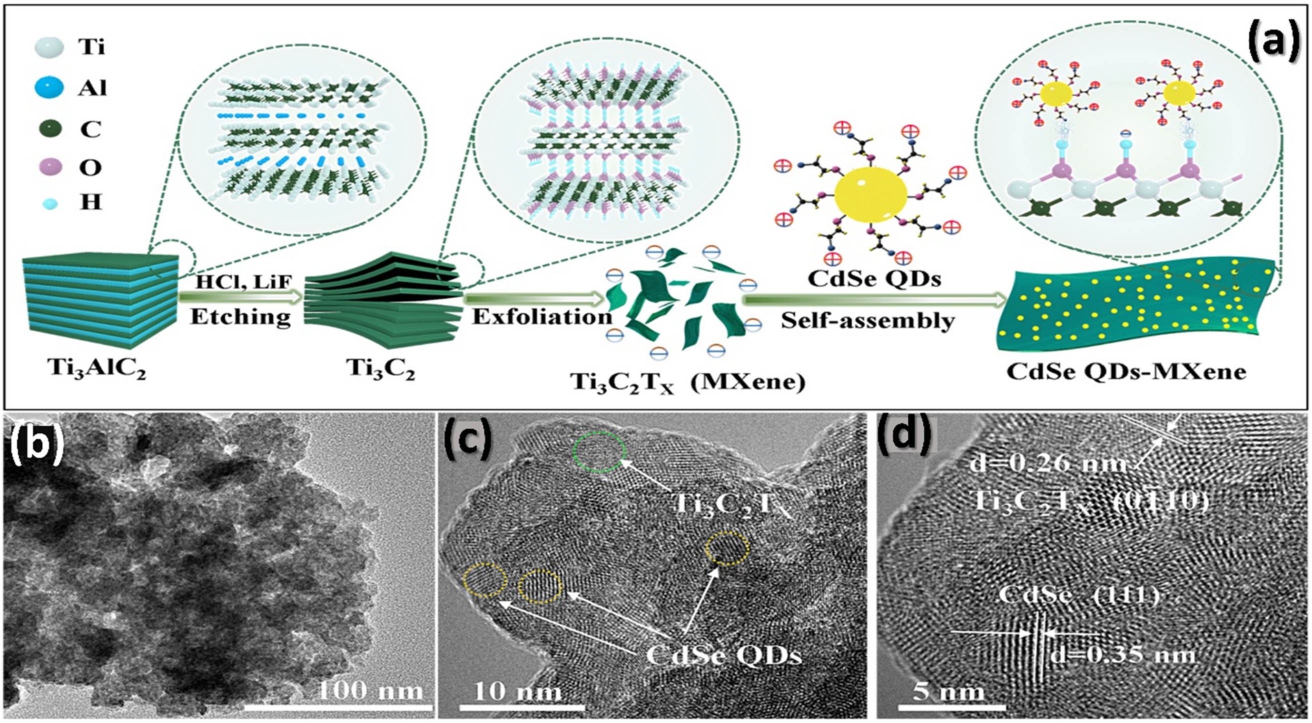

Fig. 4 (a) Schematic illustration for electrostatic self-assembly of CdSe QDs/MXene nanocomposites, (b) low magnified TEM, and (c and d) HRTEM images of the CdSe QDs–2%MXene nanocomposite. Reproduced from ref. 72 with permission from Elsevier, copyright 2021.

valuable insights into the design of heterojunction photocatalysts based on halide perovskite quantum dot materials for enhanced photocatalytic applications.

In this regard, Que *et al.* and their coworkers synthesized another hybrid material consisting of $FAPbBr_3$ QDs integrated with 2D MXene through a facile method.[92] Moreover, initial experiments revealed that formamidinium lead bromide QDs ($FAPbBr_3$ QD) exhibited superior photostability and longer electron–hole pair lifetime.[93] In the $FAPbBr_3/Ti_3C_2$ heterojunction, electron transfer from $FAPbBr_3$ to Ti_3C_2 creates a strong donor–acceptor interaction, leading to charge separation and a naturally occurring electric field at the interface. This behavior leads to other 0D–2D nanocomposites, where electron transfer enhances charge separation. As per Fig. 5(f), time-resolved PL measurements showed shorter decay lifetimes for $FAPbBr_3/Ti_3C_2$ composites compared to pure $FAPbBr_3$, indicating efficient electron transfer between $FAPbBr_3$ QDs and Ti_3C_2 nanosheets.[94,95] Again in Fig. 5(g), $FAPbBr_3$ showed an exciton bleach at 513 nm after a 400 nm pump pulse, indicating fast carrier trapping within 95 PS followed by long-lived excitons. Electrochemical impedance spectroscopy (EIS) showed that the semi-arcs in the Nyquist plots of the $FAPbBr_3/0.2\text{-}Ti_3C_2$ sample decreased in the low-frequency range. Hence, this approach has paved the way for new research in the development of metal halide perovskite-based photocatalysts.

4.5. MXene-modified platinum based quantum dots

Platinum nanoparticles (Pt NPs) are one of the most effective cocatalysts in photocatalysis, where their size determines the activity and the selectivity of the catalytic reaction. Moreover, Pt QD dispersion optimization plays a crucial role in photosynthesis with low Pt particle content. Therefore, as shown in Fig. 6(a), Devarayapalli and his group synthesized $Pt\text{–}TiO_2NW/Ti_3C_2$ heterostructures with improved interfacial bonding between the different components by the photo deposition method.[96] Again, the XPS spectral data shows the

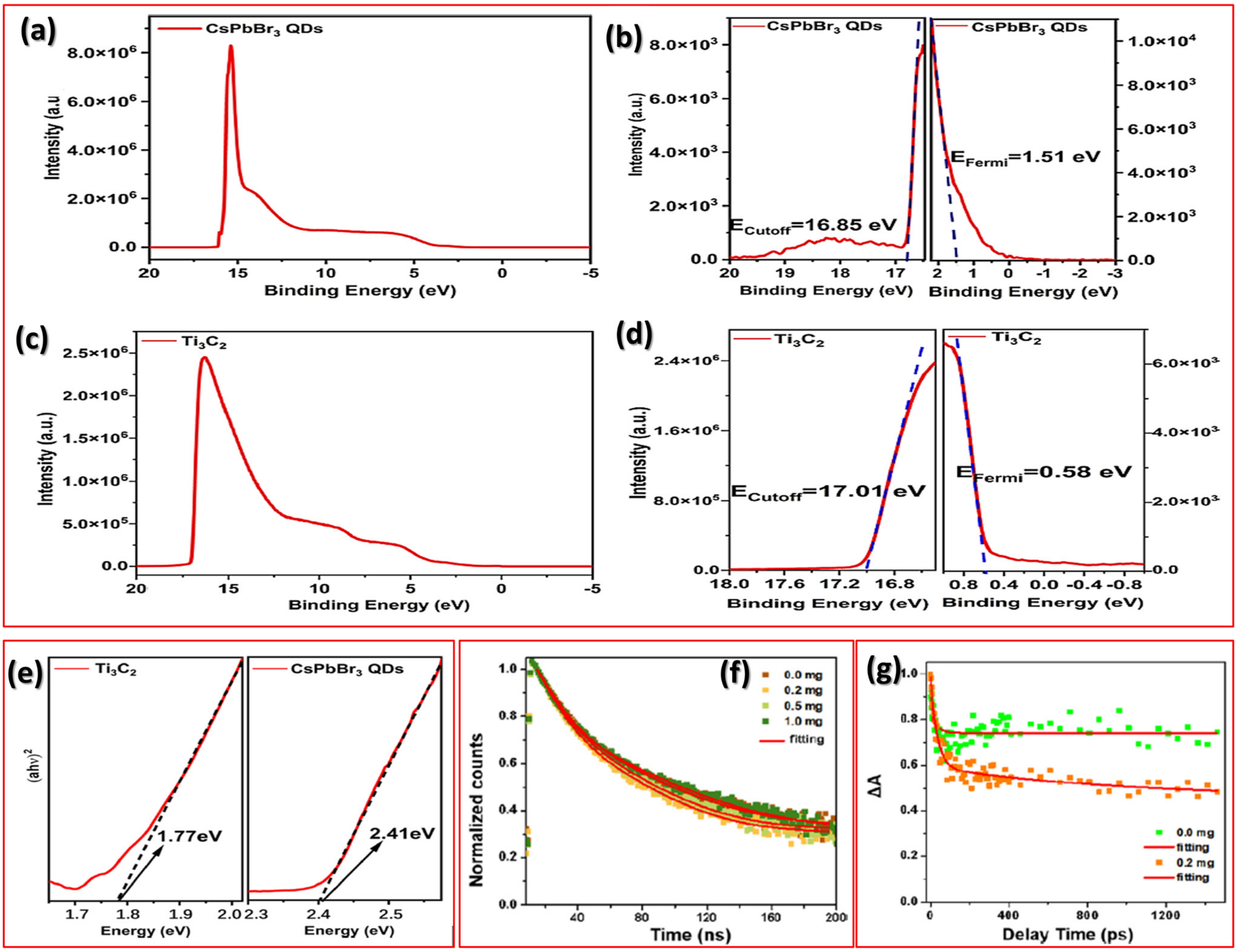

Fig. 5 UPS spectra of $CsPbBr_3$ QDs and Ti_3C_2: (a) full scan spectra of $CsPbBr_3$ QDs, (b) E_{cutoff} and E_{Fermi} of $CsPbBr_3$ QDs, (c) full scan spectra of Ti_3C_2, (d) E_{cutoff} and E_{Fermi} of Ti_3C_2, and (e) converted band gap of Ti_3C_2 and $CsPbBr_3$ QDs. Reproduced from ref. 91 with permission from American Chemical Society, copyright 2021. $FAPbBr_3/x\text{-}Ti_3C_2$ (x = 0.0, 0.2, 0.5): (f) TRPL spectra and (g) $FAPbBr_3/x/x\text{-}Ti_3C_2$ (x = 0.0 and 0.2): transient absorption kinetics. Reproduced from ref. 92 with permission from American Chemical Society, copyright 2021.

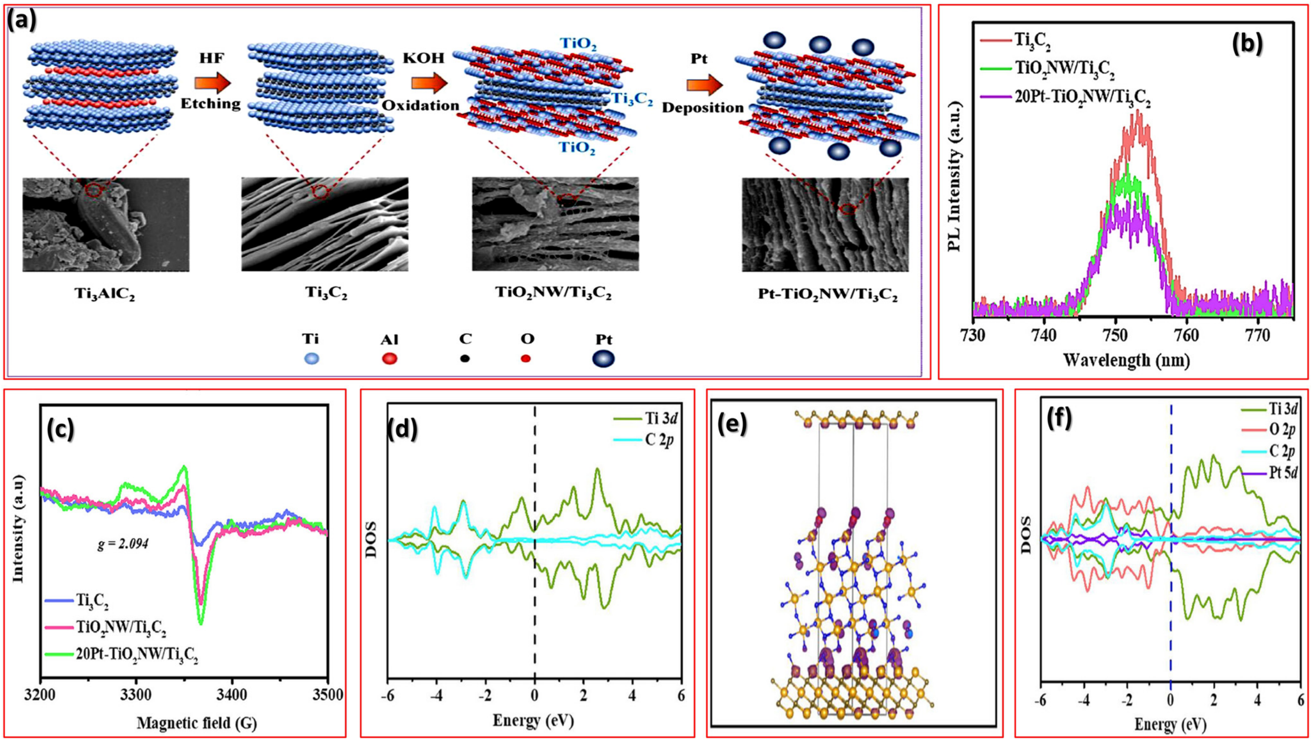

Fig. 6 (a) Schematic of the step-by-step preparation of Pt–TiO_2NW/Ti_3C_2, (b) photoluminescence emission, and (c) electron spin resonance spectra of Ti_3C_2, TiO_2NW/Ti_3C_2, and 20Pt–TiO_2NW/Ti_3C_2, (d) DOS plots of Ti_3C_2, with the partial DOSs of the Ti 3d and C 2p orbitals, and (e and f) DOS plots of Pt–TiO_2NW/Ti_3C_2, with the partial DOSs of the Ti 3d, O 2p, C 2p, and Pt 5d orbitals. Reproduced from ref. 96 with permission from Elsevier, copyright 2023.

transfer of electrons from the Pt QDs to the TiO_2NW/Ti_3C_2 surface, forming Schottky junctions that enhance charge separation rates. Importantly, the absorption edge of the TiO_2NW/Ti_3C_2 nanostructure remains largely unchanged with the addition of Pt QDs. However, a significant spectral shift in the spectrum from 461 to 456 nm in the visible light range is observed for the 20Pt–TiO_2NW/Ti_3C_2 heterostructure catalyst, which is attributed to the cocatalyst effects of the Pt quantum dot.[97,98] The energy gap (E_g) values for TiO_2NW/Ti_3C_2 and 20Pt–TiO_2NW/Ti_3C_2 are determined to be 3.31 eV and 3.23 eV, respectively, according to the UV-visible diffuse reflectance (DR) spectra. Further, the negatively charged surface of TiO_2NW/Ti_3C_2 is due to the abundance of surface termination groups, which enables better interfacial contact between the Pt QDs and TiO_2NW/Ti_3C_2.[99] Again, photoinduced carrier migration in Ti_3C_2, TiO_2NW/Ti_3C_2, and 20Pt–TiO_2NW/Ti_3C_2 catalysts was studied using photoluminescence (PL) emission and electrochemical impedance (EIS) spectroscopy as shown in Fig. 6(b and c). The 20Pt–TiO_2NW/Ti_3C_2 catalyst showed significantly higher photocurrent density, enhancing charge separation and improving photocatalytic CO_2 reduction. PL emission spectra revealed reduced PL intensity in the 20Pt–TiO_2NW/Ti_3C_2 catalyst, indicating better electron transport efficiency. Electron spin resonance (ESR) spectra showed increased oxygen vacancies in Pt-decorated TiO_2NW/Ti_3C_2, aiding electron–hole pair separation. These oxygen vacancies may effectively promote the separation of the photogenerated charge carrier pairs, enhancing CO_2 photoreduction.[100,101] Again, as per Fig. 6(d–f), the density of states (DOS) analysis reveals the electronic structures of Ti_3C_2 and Pt–TiO_2NW/Ti_3C_2, showing that Ti_3C_2 exhibits metallic behaviour due to overlapping valence and conduction bands. Pt–TiO_2NW/Ti_3C_2 exhibits higher spin states in Ti 3d orbitals, contributing to its metallic properties. The Ti, O, C, and Pt orbitals play key roles in conductivity and catalysis, with Pt influencing electron localization without changing the Fermi level's band gap. Though, the surface area of TiO_2NW/Ti_3C_2 (5.76 $m^2\ g^{-1}$) nanostructure is larger than Ti_3C_2 (4.5 $m^2\ g^{-1}$), but 20Pt–TiO_2NW/Ti_3C_2 heterostructures show decrease in surface area due to the incorporated Pt QDs covering the peripheries of the open sites, indicating that the surface is not the key factor influencing the photoactivity of the catalyst.

4.6. MXene-modified sulfur based quantum dots

Sulfur quantum dot (SQDs), since their discovery in 2014, have attracted much interest due to some special properties such as low toxicity, good optical properties and facile synthesis. Among various sulfur-based quantum dots, including cadmium sulfide (CdS) and zinc sulfide (ZnS), CdS stands out as the most efficient photocatalyst due to its suitable bandgap, appropriate bandgap position, excellent response to visible light, and controllable morphology. Moreover, Liu and his group synthesized a CdS QDs@ MXene/PVDF photocatalytic heterostructure membrane, where the XRD showed a shift in the (002) peak and an increase in crystal plane spacing, confirming successful MXene formation.[102] Moreover, AFM revealed a mean thickness of about 1.4 nm, confirming MXene's 2D lamellar nature, making it suitable for fabricating two-dimensional membranes. Similarly, as per Fig. 7(a–d) SEM analysis of M0 and M3 membranes (0, 3 represents the composition of the membranes) showed that the MXene membrane had a lamellar structure, uniformly placed on the PVDF base without any major defects. The separator layer thickness was 2 μm for M0 and 8 μm for M3, indicating that CdS QDs altered the membrane's uniformity. M3 had a rougher surface and a looser, thicker separator layer, which improved water molecule diffusion and penetration. Both M0 and M3 displayed characteristic finger-like and sponge-like pore structures. As depicted in Fig. 7(e), EDS-mapping of M3 confirmed the uniform distribution of C, S, O, Cd, and Ti, indicating that CdS QDs and MXene were evenly incorporated into the membrane. Further Fig. 7(f) represents the fabrication technique of the nanocomposite CdS QDs@ MXene/PVDF membrane.

Similarly, CdS QDs/$Ti_3C_2T_x$ nanosheets were fabricated by Yang and his group in which MXene serving as a cocatalyst, acts as a loading substrate for CdS to reduce aggregation during the SILAR method. CdS QDs/$Ti_3C_2T_x$ nanocomposites with varying amounts of CdS quantum dots were prepared using 3, 6, 9, and 12 SILAR cycles, and designated as CT-x, where x represents the number of SILAR cycles.[103] Moreover, $Ti_3C_2T_x$ and CT-9 are both 2D stacking layers with large sizes, which is shown in TEM results (Fig. 8(a and b)). Studying the Fourier transform infrared (FT-IR) spectra provides insights into the surface functionalization of the various samples. Notably, a peak at 1284 cm^{-1}, which is attributed to the stretching vibration of the covalent C–F bond in $Ti_3C_2T_x$, disappears in the CT-9 sample, indicating the replacement of –F groups by –OH during the CdS deposition process. The abundance of –OH groups on the MXene surface is beneficial, as they can enhance the electronic density of state at the Fermi level, leading to reduced resistance and improved electronic conductivity. This enhancement supports effective separation of photoinduced charge carriers. HRTEM analysis in Fig. 8(c and d) showed that $Ti_3C_2T_x$ and CT-9 have two-dimensional stacked layers, with $Ti_3C_2T_x$ coated in CdS nanoparticles. The CdS nanoparticles, sized around 30–50 nm, were more likely to agglomerate without $Ti_3C_2T_x$, but the presence of $Ti_3C_2T_x$ reduced this agglomeration and controlled the size of the CdS particles. Additionally, the semicircle radius of CT-9 is considerably smaller than that of CdS, suggesting enhanced charge separation following the

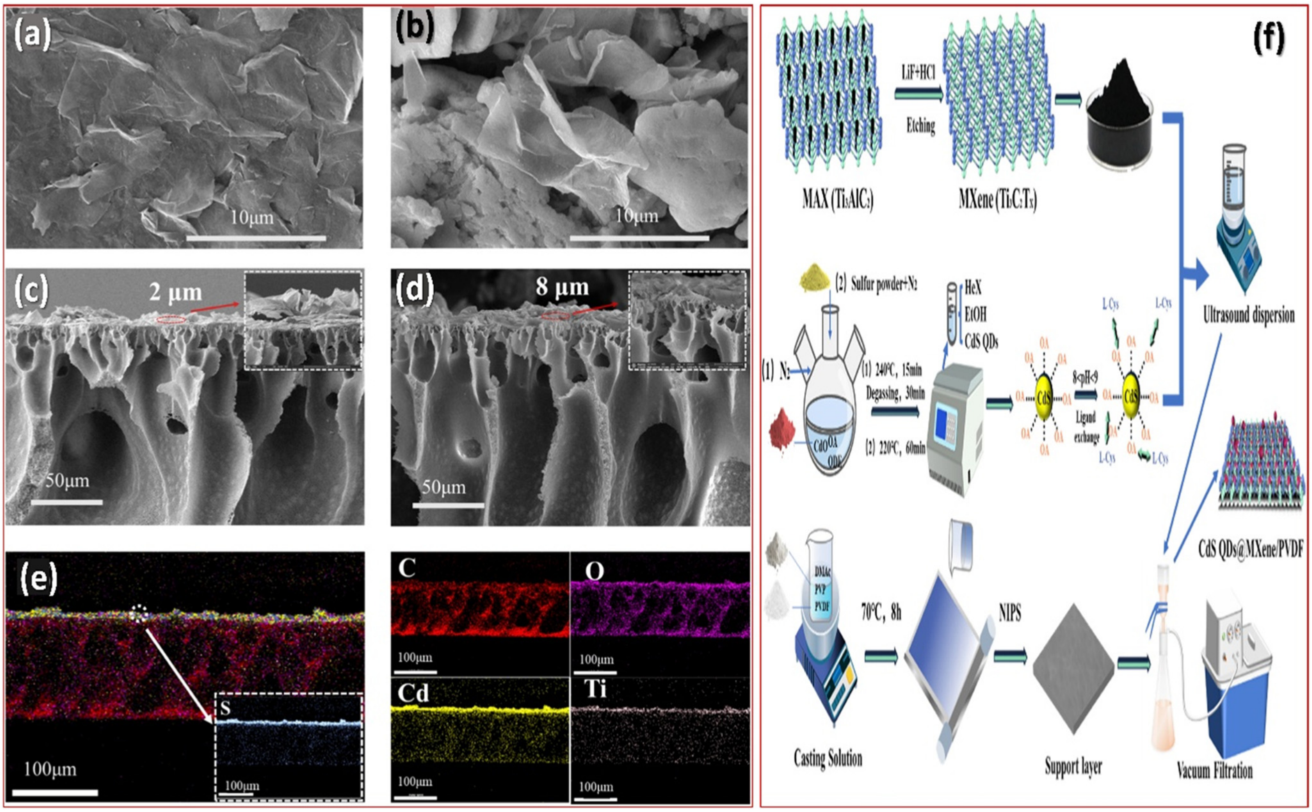

Fig. 7 Top-down SEM images of M0 (a) and M3 (b), cross-sectional SEM images of M0 (c) and M3 (d) (insets are enlarged cross-sectional images of the corresponding membrane), (e) EDS-mapping of M3, and (f) CdS QDs@ MXene/PVDF membrane fabrication. Reproduced from ref. 102 with permission from Elsevier, copyright 2024.

incorporation of $Ti_3C_2T_x$. This improvement in charge transfer efficiency underscores the beneficial role of $Ti_3C_2T_x$ in the composite. Therefore, the CdS QDs/$Ti_3C_2T_x$ composite demonstrates enhanced photocatalytic activity compared to pure CdS, with the optimal CT-9 catalyst achieving high effectiveness in the degradation of carbamazepine (CBZ) under simulated sunlight irradiation.

4.7. MXene-modified carbon-based quantum dots

Carbon quantum dots (CQDs) have been extensively applied in numerous fields such as chemical sensing, bioimaging, drug delivery, and photocatalysis. They have garnered significant attention due to their excellent, efficient electron transport, aqueous solubility, and exceptional light-harvesting capabilities, enabling full solar spectrum utilization. Further, green CQDs are drawing increasing attention because of their nontoxic nature, higher compatibility, good dispersibility, and outstanding chemical stability. Moreover, Zahedi *et al.* synthesized a carbon quantum dot (CQD) based heterostructure in combination with $Ti_3C_2(OH)_2$ MXene (CQDs/MXene) for rapid photodegradation of malachite green (MG) under visible light irradiation.[104] Again, Fig. 8(e and f) shows FE-SEM images of MXene and its CQDs/MXene composite, revealing that the compact, sheet-like morphology of MXene remained unchanged after composite formation. Further, energy dispersive X-ray (EDX) analysis of the CQDs/MXene composite confirmed the presence of carbon, oxygen, nitrogen, aluminum, and titanium elements, with respective abundances of 30%, 23.89%, 16.99%, 6.72%, and 22.40%. Similarly, as shown in Fig. 8(g), the XRD analysis confirmed the formation of $Ti_3C_2(OH)_2$ MXene after washing and drying and exhibits characteristic peaks at 38° and 40°. A titanium phase was also detected in the CQDs/MXene pattern. The XRD of MXene prepared by the hydrothermal method exhibited a broad peak at 28°, indicating $Ti_3C_2T_x$, and sharp peaks in the catalyst pattern indicated good crystallization of the nanocomposite.

5. Applications of MXene-modified QD composites for various photocatalytic applications

5.1. Photocatalytic H_2 evolution

The reliance on fossil fuels as a primary energy source leads to significant ecological challenges and is a key contributor to human-induced climate change. The environmental impact of fossil fuel dependence is closely linked to these challenges, emphasizing the need for sustainable alternatives. Hydrogen, as a cleaner and renewable energy source, offers a promising solution with its large energy density of 143 kJ g^{-1} and the absence of secondary pollution.

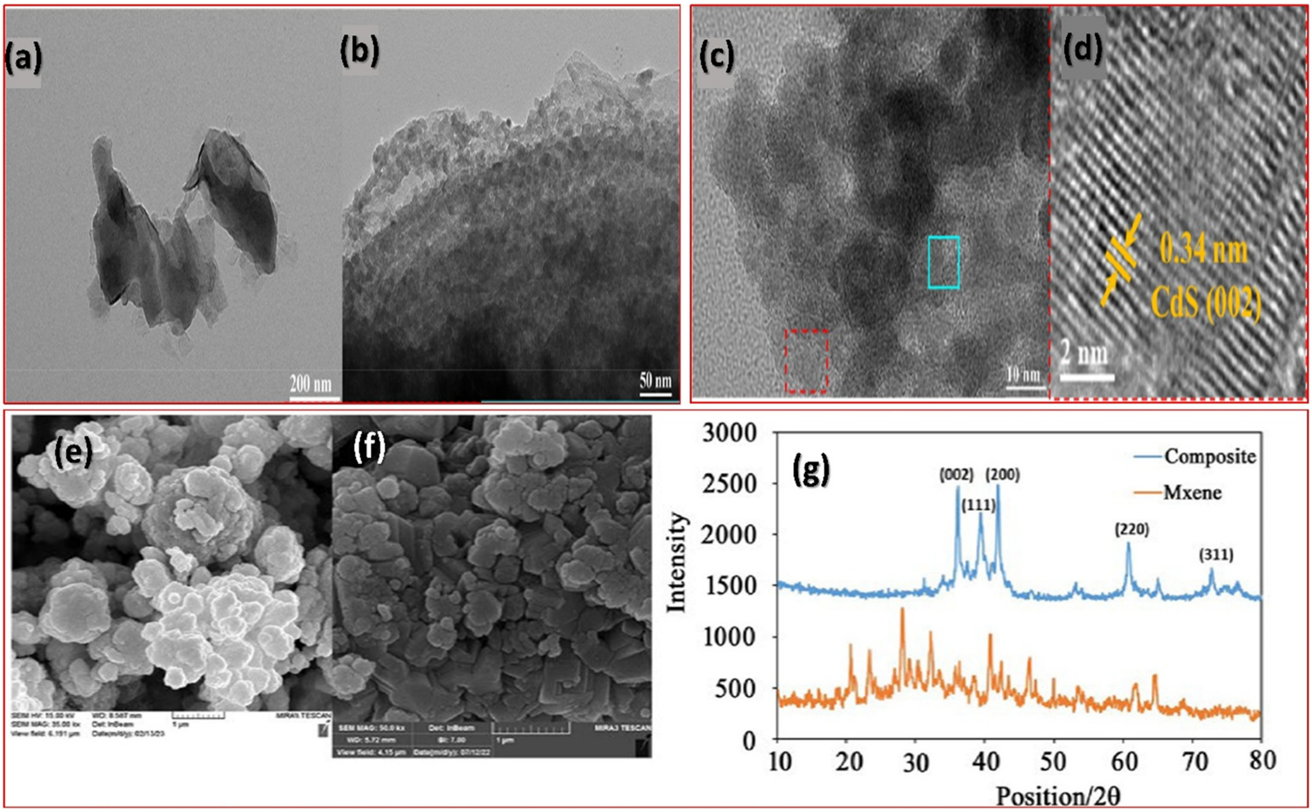

Fig. 8 TEM images of (a) $Ti_3C_2T_x$ and (b) CT-9 and (c and d) HRTEM images of CT-9.[103] SEM images of (e) MXene (left) and (f) nanocomposite (right); (g) XRD patterns. Reproduced from ref. 104 with permission from American Chemical Society, copyright 2023.

Hydrogen can be produced through three main strategies: biofuels, fossil fuels, and water splitting. However, hydrogen production from fossil fuels generates CO_2 as a byproduct, contributing to environmental pollution, and biological hydrogen production at a large scale remains costly. In contrast, hydrogen production *via* water splitting using wastewater is an eco-friendly and sustainable approach. A landmark discovery by Fujishima and Honda in 1972 demonstrated hydrogen evolution through photoelectrochemical water splitting using TiO_2 electrodes under UV irradiation.[105] This groundbreaking finding sparked considerable scientific interest in photocatalytic hydrogen generation through water splitting. As a result, significant advancements have been made in developing various solar-active photocatalysts, including TiO_2, ZnO, CuO, ZnS, CdS, and WO_3, to enhance the efficiency of this process and meet future energy demands.

Based on natural photosynthesis, directly converting solar energy into valuable fuels offers a promising strategy to resolve the global energy crisis. During the photocatalytic reactions, three primary steps are majorly involved: (i) the photocatalyst absorbs light and evolved charge carriers (electron–hole pairs); (ii) charge segregation and transfer through the bulk of the photocatalyst; and (iii) the generated exciton pairs transfer through the surface of the bulk photocatalyst to participate in conjugative oxidation and reduction photocatalytic reactions (Scheme 2). In this process, a successful charge separation occurs when exciton pairs migrate to the catalytic surface without recombination. At the surface, oxidation occurs at the VB using the generated holes to oxidize water, producing protons and oxygen, while reduction takes place at the CB, where electrons reduce protons to generate hydrogen. As outlined in the reactions below, certain redox conditions must be met for efficient hydrogen production (eqn (1)–(3)).[105–107]

$$\text{Oxidation: } 2H_2O \rightarrow O_2 + 4H^+ + 4e^- \quad E^0 = 1.23\ \text{eV} \tag{1}$$

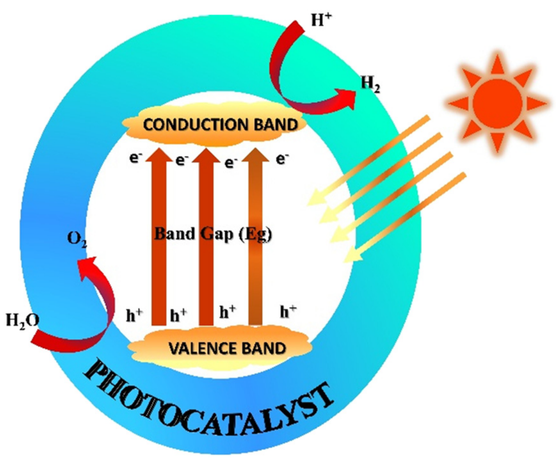

Scheme 2 Schematic representation of photocatalytic hydrogen evolution.

$$\text{Reduction: } 2H^+ + 2e^- \rightarrow H_2 \quad E^0 = 0.00\ \text{eV} \tag{2}$$

$$\text{Overall: } 2H_2O \rightarrow O_2 + 2H_2 \quad E^0 = 1.23\ \text{eV} \tag{3}$$

Ti_3C_2 MXenes possess several significant properties, including excellent electrical conductivity, high thermal stability, favourable optical characteristics, and versatile surface termination groups, making them a perfect candidate for coupling with other semiconductors to improve photocatalytic performance. The charge transfer mechanism between MXene and the semiconductor depends on the relative work function of MXene with respect to the semiconductor. Based on this relationship, different charge transfer pathways, such as Schottky junction formation, ohmic contact, or band alignment adjustments, have been proposed to optimize charge separation and enhance photocatalytic performance. With Ti_3C_2 acting as a cocatalyst alongside a semiconductor, a Schottky junction forms, which helps separate charge carrier pairs. The close and intense interaction between MXenes and the semiconductor creates a Schottky barrier, resulting in strong interfacial charge accumulation across the metal–semiconductor boundary. Under light illumination, the semiconductor absorbs photons, leading to electron excitation from the valence band (VB) to the conduction band (CB), generating exciton pairs. Due to their higher work function and lower Fermi level compared to the semiconductor, MXenes serve as electron acceptors. Electrons migrate from the semiconductor (with a larger Fermi level) to the MXene until their Fermi levels become aligned, promoting charge separation and enhancing the efficiency of photocatalytic processes such as water splitting. DFT calculations have shown that O-terminated Ti_3C_2 has a near-zero Gibbs free energy for hydrogen adsorption (DGH) and the most positive value of EF, indicating high H_2 evolution activity and the capability to capture photo-induced electrons.

5.1.1 MXene-modified QD heterostructures for photocatalytic H_2 evolution. To boost photocatalytic efficiency, MXene plays the role of a co-catalyst for various semiconductors that construct a binary heterostructure. Recently, MXene has gained extensive attention in photocatalysis due to its superior electron-capturing ability, which effectively facilitates efficient charge carrier separation. In this advancement, Ti_3C_2 MXenes are mainly introduced as co-catalysts in photocatalytic water splitting, having higher H_2 yields as compared to pure semiconductor materials. MXene materials are metallic with the Fermi level near the valence band center. Their work function, ranging from 3.5 eV to 5 eV, is influenced by surface terminations. Oxygen-terminated MXenes typically have a higher work function, indicating that surface chemistry significantly affects electron removal. In this regard, Qi *et al.* fabricated a Ti_3C_2 MXene-modified TiO_2 QD binary heterostructure for photocatalytic H_2 evolution.[73] In this preparation strategy, small-sized TiO_2 photocatalysts were attached to large-sized MXene nanosheets, which offer a large number of active sites for capturing photoinduced electrons. The metallic MXene effectively captures photo-excited electrons from small-sized TiO_2 to obtain rapid charge segregation. Further to examine the photocatalytic properties of TiO_2@MXene composites, Fig. 9(a) shows the hydrogen production, where a linear relation between hydrogen production and reaction time can be clearly observed. Maintaining the 4 h-hydrogen production duration, the optimum photocatalysts showed a higher H_2 production yield compared to pristine TiO_2 (Fig. 9(b and c)). Again, as per Fig. 9(d and e), ESR signals are minimal without light (dark conditions). Similarly, Fig. 9(f) demonstrates the LSV curves of TiO_2 QDs, MXene nanosheets, and the optimized composite, exhibiting a lower onset potential of hydrogen evolution than that of TiO_2 QDs. Moreover, Fig. 9(g) represents the schematically proposed photocatalytic mechanism elucidated through spectroscopic and electrochemical data.

Moreover, due to their unique characteristics, transition metal chalcogenide quantum dots (TMCs QDs) show great potential for solar energy harvesting and utilization. Still, their instability and charge carrier recombination limit their effectiveness. In this regard, 0D/2D CdSe QDs/MXene nanocomposites were developed using a ligand-initiated electrostatic self-assembly approach, where CdSe QDs were anchored on $Ti_3C_2T_x$ MXene nanosheets.[72] The CdSe QDs–2%M nanocomposite undergoes considerably boosted performance in photocatalytic reduction for H_2 generation under visible light, compared to pristine CdSe QDs. This enhancement contributes to MXene's role as an electron trap, facilitating unidirectional electron flow from CdSe QDs to MXene, which prolongs charge lifetimes and improves stability under light irradiation. As depicted in Fig. 10(a), blank CdSe QDs exhibit a low photocatalytic H_2 evolution rate of 91 μmol h^{-1} g^{-1}, which will increase with a larger loading amount of $Ti_3C_2T_x$ MXene NSs. Further, among the different agents such as ethanol, methanol, glycerol, ethylene glycol, and lactic acid, lactic acid exhibited the maximum efficiency, attributed to its strong deprotonation ability, which effectively alters the surface behavior of the photocatalytic heterostructure and controls the complete adsorption process (Fig. 10(b)). Fig. 10(c) shows that the photocatalytic activity of CdSe QDs–2%M increases with rising light intensity, demonstrating that a photocatalytic process drives the H_2 evolution reaction. Moreover, based on the above results, the photocatalytic mechanism of CdSe QDs–2%M is illustrated in Fig. 10(d). This finding offers new insights into 0D–2D hybrid nanoarchitectures, where intimate interfacial contacts and well-aligned energy levels are crucial for boosting photocatalytic hydrogen evolution efficiency.

Moving towards ternary heterostructures, Liu *et al.* constructed a BPQDs/Ti_3C_2@TiO_2 photocatalyst, where TiO_2 nanoparticles were *in situ* grown on Ti_3C_2 MXene nanosheets and modified with black phosphorus quantum dots (BPQDs) to form a ternary heterojunction nanostructure.[77] The BPQDs/Ti_3C_2@TiO_2-120 composite exhibits optimized photocatalytic performance, with a hydrogen evolution rate of 684.5 μmol h^{-1} g^{-1} under

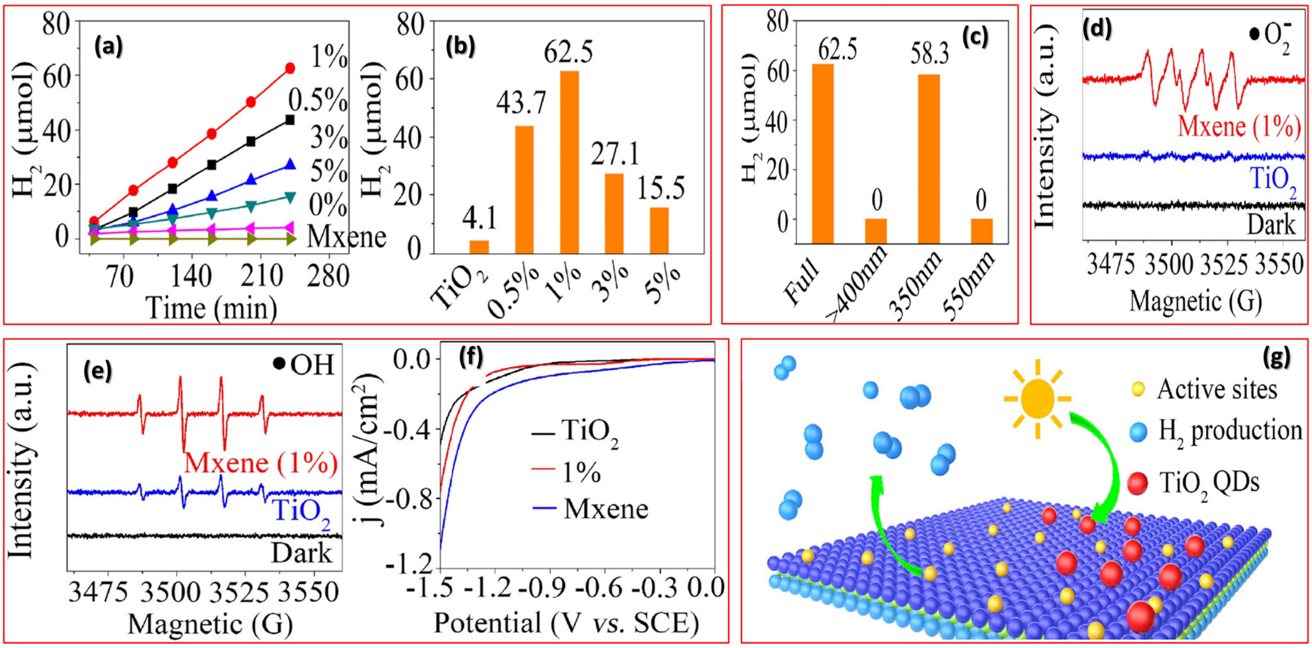

Fig. 9 (a) Photocatalytic hydrogen production of TiO_2 QDs coupled with different concentrations of MXene nanosheets as a function of reaction time, (b) photocatalytic hydrogen production for 4 h, (c) photo-catalytic hydrogen production for 4 h with band-pass filters for the optimized composite, (d and e) ESR spectra of TiO_2 QDs and the optimized composite for capturing ·OH and $·O_2^-$ radicals, (f) LSV curves of TiO_2 QDs, MXene nanosheets and the optimized composite, and (g) proposed photocatalytic mechanism. Reproduced from ref. 73 with permission from Elsevier, copyright 2021.

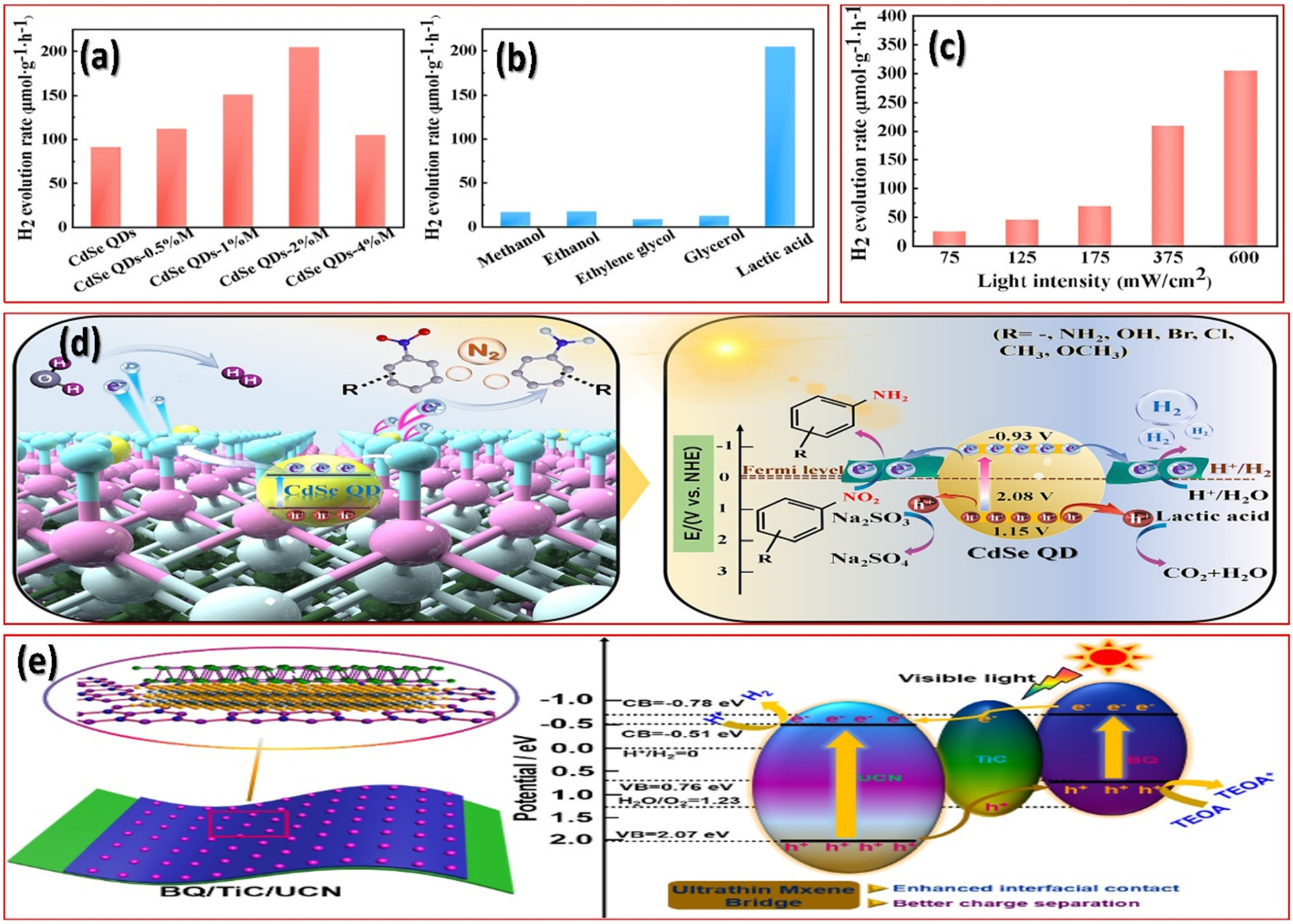

Fig. 10 (a) Photoactivities of CdSe QDs–MXene nanocomposites with different percentages of MXene toward hydrogen production under visible light ($\lambda > 420$ nm) irradiation, (b) photocatalytic hydrogen production performances of CdSe QDs–2%M in the presence of different sacrificial reagents, (c) photocatalytic hydrogen production performances of CdSe QDs–2%M under visible light irradiation with different light intensities, and (d) schematic illustration of the photocatalytic mechanism of CdSe QDs–M nanocomposites. Reproduced from ref. 72 with permission from Elsevier, copyright 2021. (e) A possible mechanism for the photocatalytic H_2 evolution over the BQ/TiC/UCN composite. Reproduced from ref. 79 with permission from Elsevier, copyright 2020.

visible light, outperforming other samples. Photogenerated electrons migrate from the conduction band (CB) of BPQDs to TiO_2 and then to Ti_3C_2, facilitated by the surface heterojunction, enhancing the efficiency of carrier separation and transport. Additionally, the larger surface area of BPQDs/Ti_3C_2@TiO_2 provides many active sites for the photocatalytic process. This structure significantly boosts photocatalytic hydrogen evolution, offering a promising approach for energy applications. Similarly, Deng and his co-worker modified metal-free BPQDs/g-C_3N_4 (UCN) with ultrathin Ti_3C_2 MXene-based photocatalysts through an uncomplicated approach.[79] The TiC nanosheets are combined with black phosphorus (BQ) and ultrathin UCN to form a 0D/2D heterojunction, enhancing photocatalytic hydrogen production. The fine-tuned BQ/TiC/UCN composite demonstrates intimate interfacial contact and optimized visible-light absorption, significantly accelerating charge transfer and exciton pair separation. Consequently, the composite with an AQY of 17.6% at 420 nm exhibits 47.2 times and 19.4 times larger photocatalytic activity than pristine g-C_3N_4 and ultrathin g-C_3N_4, respectively. Moreover, the composite demonstrated excellent stability after six consecutive reactions, confirmed by FTIR and XRD analyses. Based on the above results, a possible mechanism explaining the outstanding HER performance of BQ/TiC/UCN is proposed and illustrated in Fig. 10(e). This work provides valuable insights into MXene-based catalysts for improving solar energy utilization. Table 1 summarizes the photocatalytic hydrogen evolution of MXene Ti_3C_2-modified QD nanocomposites under different experimental conditions.

5.2. Photocatalytic CO_2 reduction

CO_2 reduction *via* photocatalysis to produce valuable chemicals is essential for lowering greenhouse gas concentrations and fulfilling the need for renewable fuels.

Table 1 Represents the photocatalytic activity of MXene-modified QD nanocomposites towards various photocatalytic applications

SL no.	Type of MXene modified systems	Photocatalyst	Method	Photocatalytic reaction condition	Photocatalytic activity of pristine materials	Photocatalytic applications	Reference
1.	MXene modified phosphorous-based QD	BQ/TiC/UCN	Mixing and ultrasonication	Light source (300 W Xe lamp), sacrificial reagent (triethanolamine (10 vol%))	UCN-0.95 mmol g^{-1} h^{-1}, TiC/UCN-3.08 mmol g^{-1} h^{-1} (UCN-g-C_3N_4)	Hydrogen evolution (18.42 mmol h^{-1} g^{-1})	79
2.	MXene modified phosphorous-based QD	BPQDs/Ti_3C_2/TiO_2	Hydrothermal	Light source (300 W Xe lamp), sacrificial reagent (triethanolamine)	TTC (Ti_3C_2/TiO_2) 120–324.5 μmol h^{-1} g^{-1}, BTC (BPQDs/Ti_3C_2) sample – 60.3 μmol h^{-1} g^{-1}	Methyl orange (MO) degradation (93%) and hydrogen evolution (684.5 μmol h^{-1} g^{-1})	77
3.	MXene modified oxide-based QD	NiO QDs/TiO_2/Ti_3C_2	Thermal decomposition	Light source (500 W Xe lamp)	—	Rhodamine B (Rh B) degradation	93
4.	MXene modified oxide-based QD	TiO_2 QDs/Ti_3C_2	Hydrothermal	Light source (300 W Xe lamp), sacrificial reagent (triethanolamine)	Pure TiO_2–4.1 μmol h^{-1} g^{-1}	Hydrogen evolution (62.5 μmol h^{-1} g^{-1})	73
5.	MXene modified selenide-based QD	TMCs QDs/Ti_3C_2	Self-assembled	Light source (300 W Xe lamp), sacrificial reagent (lactic acid)	Blank CdSe QDs-91 μmol h^{-1} g^{-1}	Hydrogen evolution (204 μmol h^{-1} g^{-1})	72
6.	MXene modified inorganic halide perovskites-based QD	$FAPbBr_3$/Ti_3C_2	Physical mixing	Light source (300 W Xe lamp)	Pristine $FAPbBr_3$ QDs-343.90 μmol h^{-1} g^{-1}	CO_2 reduction (717.18 μmol g^{-1} h^{-1})	92
7.	MXene modified inorganic halide perovskites-based QD	Ti_3C_2/$CsPbBr_3$ QD	Self-assembly method	Light source (300 W Xe lamp)	$CsPbBr_3$ QDs −1.92 μmol h^{-1} g^{-1}	CO_2 reduction (17.98 μmol h^{-1} g^{-1})	91
8.	MXene modified platinum-based QD	PtQDs-TiO_2NW/Ti_3C_2	Photo-deposition	Light source (300 W Xe lamp)	TiO_2NW/Ti_3C_2 (CO: 32.16 μmol h^{-1} g^{-1} and CH_4: 25.89 μmol h^{-1} g^{-1} after 10 h of irradiation)	Carbon dioxide reduction (CO and CH_4 production: 38.14 and 36.12 l mol g^{-1})	96
9.	MXene modified sulphur-based QD	CdS QDs/$Ti_3C_2T_x$	SILAR method	Light source (300 W Xe lamp)	—	Carbamazepine (CBZ) degradation (95.2%)	103
10.	MXene modified sulphur-based QD	CdS QDs/Ti_3C_2/PVDF	Vacuum-assisted self-assembly	Light source (365 W Xe lamp)	—	Organic dyes (97.3% for Congo red (CR) and 98.5% for Rhodamine B (Rh B))	102
11.	MXene modified carbon-based QD	CQDs/Ti_3C_2	Self-assembly process	Light source (300 W Xe lamp)	—	Malachite green degradation (96.1%)	104

CO_2 photoconversion research began in the late 1970s, with early studies conducted by Halmann.[108] Artificial photosynthesis using semiconductor photocatalysts to convert CO_2 into various chemicals is essential for addressing energy needs and mitigating climate change. Converting CO_2 into hydrocarbon fuels is a viable solution to resolve environmental and energy concerns. As a result, extensive research has been conducted on various semiconductor materials for the photocatalytic reduction of CO_2. Semiconductors such as TiO_2, GaN, Fe_2O_3, WO_3, ZnO, and g-C_3N_4 have been studied for their ability to reduce CO_2 into products like CH_3OH, HCHO, HCOOH, CO, and CH_4. Carbon dioxide is a highly stable and unreactive compound because of the robust nature of the C=O double bond, which has an energy of 750 kJ mol^{-1}, and this stability necessitates high temperatures and pressures for its thermos catalytic conversion. The cleavage of the stable C=O double bond (750 kJ mol^{-1}) requires using an external photosensitizer and CO_2 activation co-catalysts, which effectively facilitate the photocatalytic process. Photocatalytic activation of CO_2 has the potential to be a more environmentally friendly process, as it can be performed at lower temperatures and pressures, reducing energy consumption. The redox potential associated with the single electron reduction of CO_2 is −1.85 eV (*vs.* NHE at pH = 7), making the process unfavorable due to the difficulty in bending the linear CO_2 molecule and injecting an electron and this potential is more negative than the conduction band edge of the majority of semiconductors (Scheme 3). However, some specific photocatalysts can bind CO_2 in a bent configuration, which enhance electron transport to form the CO_2^- anion. An effective photocatalyst should generally have excellent charge separation, fast charge transfer, high stability, low cost, absorption within the visible spectrum range, and nontoxicity. By emulating the photosynthesis process of green plants, CO_2 can be artificially transformed into clean fuels such as CO, CH_3CH_2OH, CH_4, CH_3OH, and HCOOH through the photocatalytic process (eqn (4)–(8)).[109–112]

$$CO_2 + 2H^+ + 2e^- \rightarrow HCOOH \quad E^0 = -0.66\ V \tag{4}$$

$$CO_2 + 2H^+ + 2e^- \rightarrow CO + H_2O \quad E^0 = -0.53\ V \tag{5}$$

$$CO_2 + 4H^+ + 4e^- \rightarrow CH_2O + H_2O \quad E^0 = -0.49\ V \tag{6}$$

$$CO_2 + 6H^+ + 6e^- \rightarrow CH_3OH + H_2O \quad E^0 = -0.40\ V \tag{7}$$

$$CO_2 + 8H^+ + 8e^- \rightarrow CH_4 + 2H_2O \quad E^0 = -0.24\ V \tag{8}$$

Furthermore, effective production of desirable hydrocarbon fuels requires that the reduction potentials of CH_4 (−0.24 V) and CO (−0.53 V) be well-matched with the conduction band potential (E_{CB}) of the photocatalyst.[113] Research nowadays has emphasized the potential of Ti_3C_2 as a highly efficient co-catalyst in CO_2 photoreduction, because of its excellent electrical conductivity, high structural stability, and effective surface functionalization.[114–118] Specifically, the –OH groups on Ti_3C_2 provide numerous basic sites that enhance the adsorption and activation of carbon dioxide molecules, leading to significant improvements in CO_2 photoconversion. MXene-supported semiconductor photocatalysts can significantly improve the efficiency of photogenerated charge carrier separation while maintaining their intrinsic redox capabilities.

5.2.1 MXene-modified QD heterostructures for photocatalytic CO_2 reduction. Numerous studies have reported MXene-modified quantum dot (QD) nanocomposites for photocatalytic CO_2 reduction, highlighting their wide range of potential applications. Ti_3C_2 MXene, recognized for its excellent optical properties and enhanced electronic conductivity, has emerged as a highly promising noble metal-free co-catalyst for boosting the efficiency of photocatalysts in CO_2 reduction. In this regard, Que and his co-worker synthesized a $FAPbBr_3/Ti_3C_2$ composite that was successfully prepared through a simple process and tested as a visible-light-responsive heterostructure for CO_2 reduction in purified water.[92] Fig. 11(a) shows that adding Ti_3C_2 significantly enhances the CO_2 reduction performance of $FAPbBr_3$ QDs, with the $FAPbBr_3/0.2\text{-}Ti_3C_2$ sample achieving the highest CO yield, which is 1.84 times greater than that of the pristine QDs. Additionally, the composite showed a notable improvement in photocurrent density, from 0.034 to 0.170 μA cm^{-2}, indicating enhanced charge separation and transfer. Optical analysis demonstrated that $FAPbBr_3$ quantum dots were attached to Ti_3C_2 nanosheets *via* a Schottky heterojunction, facilitating efficient photogenerated charge separation and transfer. The performance improvements were attributed to the construction of the Schottky contact, which enhanced photocatalytic activity. Moreover, the photocatalytic mechanism of $FAPbBr_3/Ti_3C_2$ is illustrated in Fig. 11(b). This work suggests a promising new avenue for the advancement of metal halide perovskite-based heterostructures. For instance, Liu *et al.* fabricated a novel $Ti_3C_2/CSPbBr_3$ QD binary composite *via* a self-assembly method, exhibiting exceptional photocatalytic CO_2 reduction performance.[91] Fig. 11(c and d) shows that CH_4 is the dominant product in CO_2 photoreduction by $CsPbBr_3$ QDs, while Ti_3C_2 shows lower overall yields of both CO and CH_4 after 5 hours of light irradiation. Again, Fig. 11(e) demonstrates that the CH_4 yield shows limited improvement, likely due to competition with CO formation, as both products compete for photoinduced electrons. The composites achieve high yields of CO (17.98 μmol h^{-1} g^{-1}) and CH_4 (19.31 μmol h^{-1} g^{-1}), with 98.42% and 97.35%

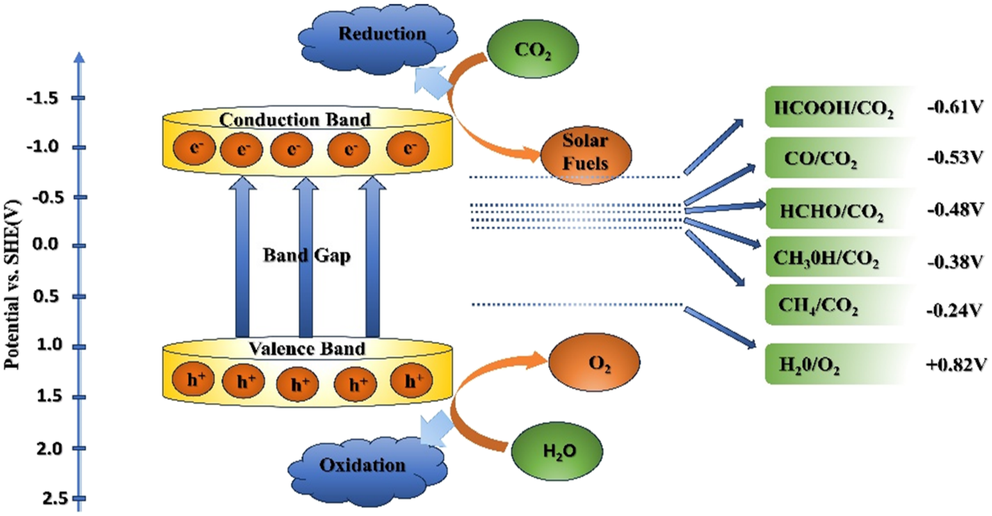

Scheme 3 Schematic representation of carbon dioxide reduction.

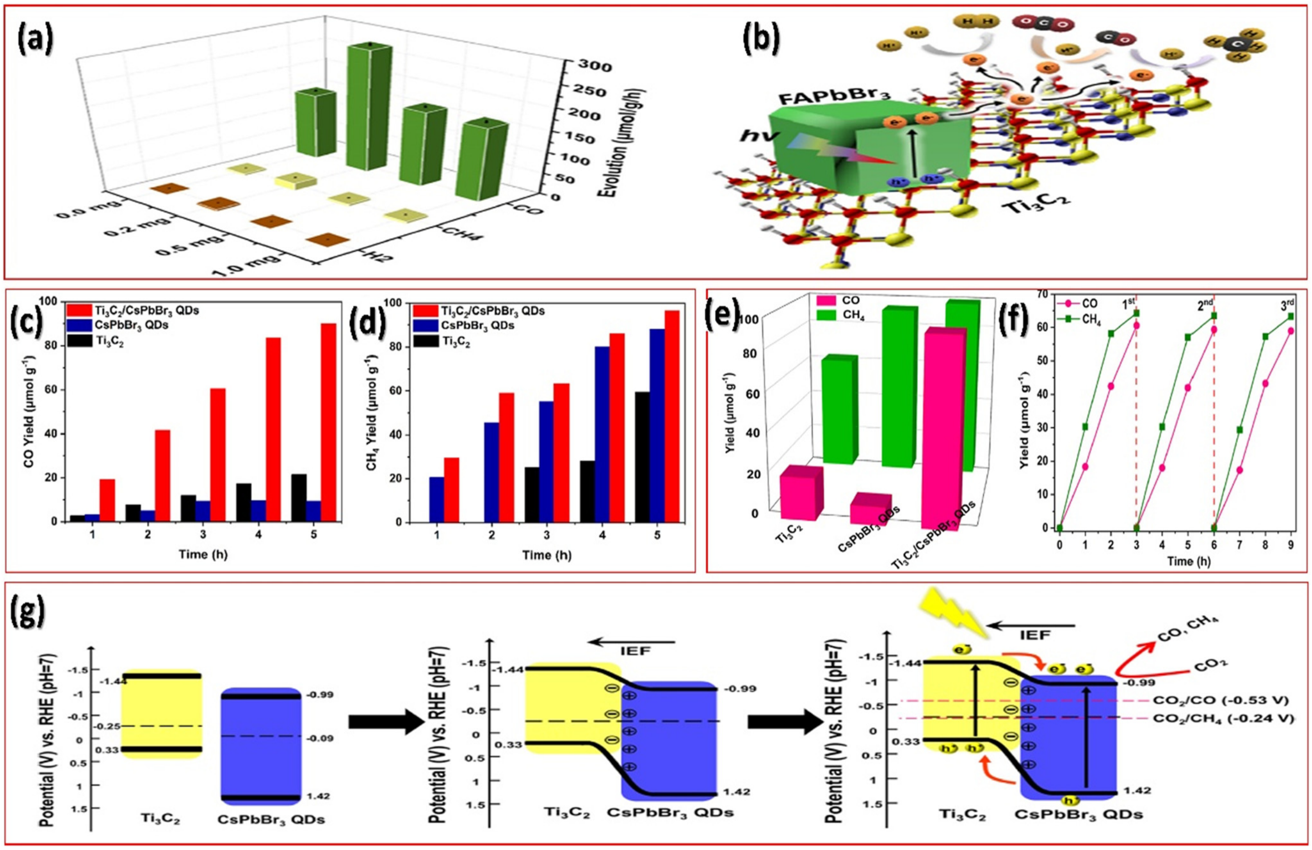

Fig. 11 (a) Photocatalytic CO_2 reduction performances in deionized water of $FAPbBr_3/x\text{-}Ti_3C_2$ (x = 0.0, 0.2, 0.5, and 1.0) under AM 1.5G (150 mW cm^{-2}), (b) Schottky heterojunction photocatalytic system for CO_2 reduction in $FAPbBr_3/x\text{-}Ti_3C_2$. Reproduced from ref. 92 with permission from American Chemical Society, copyright 2021. CO_2 photoreduction yields of Ti_3C_2, $CsPbBr_3$ QDs, and $Ti_3C_2/CsPbBr_3$ QD composites after light irradiation of 5 h: (c) CO, (d) CH_4, and (e) combined, (f) cycling stability test of $Ti_3C_2/CsPbBr_3$ QD composites after light irradiation of 3 h, and (g) type II-2 heterojunction of the $Ti_3C_2/CsPbBr_3$ QD composites: before contact, after contact, and after contact upon irradiation and charge migration and separation respectively. Reproduced from ref. 91 with permission from American Chemical Society, copyright 2021.

retention of photocatalytic activity after three cycles, respectively (Fig. 11(f)). The improved performance is due to superior light absorbance, the formation of a type II heterojunction with the existence of the IEF fields, and the unique 0D/2D structure of the composites, which improve electron–hole separation and facilitate efficient CO_2 reduction by providing a larger surface area and a greater number of active sites. Again, Fig. 11(g) shows that the $Ti_3C_2/CsPbBr_3$ QD composites form a type II-2 heterojunction, enabling effective charge transfer and separation, as shown by their band positions and Fermi level alignment. These factors combine to make $Ti_3C_2/CsPbBr_3$ QD composites promising candidates for sustainable photocatalytic applications. By utilizing MXene in this way, the photocatalyst can exhibit enhanced light absorption, greater charge carrier mobility, and improved catalytic performance, making it a promising co-catalyst in various photocatalytic applications, including carbon dioxide reduction.

Devarayapalli *et al.* prepared TiO_2NW/Ti_3C_2 binary metal oxide phases that were synthesized through the oxidation of Ti_3C_2 MXene, and the effect of incorporating Pt quantum dots (PtQDs) onto these nanostructures was investigated.[96] By employing a simple one-pot oxidation process, PtQDs were effectively bound to the TiO_2NW/Ti_3C_2 surfaces, substantially enhancing CO_2 photoreduction performance. The electronic structure analysis of the $20Pt\text{–}TiO_2NW/Ti_3C_2$ catalyst revealed conducting properties, with the Ti 3d, O 2p, C 2p, and Pt 5d orbitals playing key roles in the catalytic activity. The optimized $20Pt\text{–}TiO_2NW/Ti_3C_2$ catalyst demonstrated a 4.8-fold improvement in CO (38.14 μmol g^{-1}) and CH_4 (36.12 μmol g^{-1}) production compared to bulk Ti_3C_2 MXene. The improvement was due to the efficient integration of PtQDs, which enhanced solar-light absorption, promoted photoinduced exciton pairs, and improved catalytic efficiency, as confirmed by various characterization techniques. This strategy offers a promising approach for improving highly efficient photocatalysts for CO_2 reduction. Table 1 summarizes the photocatalytic CO_2 reduction of the MXene Ti_3C_2-modified QDs nanocomposite under different experimental conditions.

5.3. Photocatalytic pollutant degradation

With the rapid advancement of industrialization and population growth, energy crises and environmental pollution have emerged as progressively critical global challenges. Historically, industrial progress and environmental protection have often been at odds.[119] However, with growing emphasis on environmental concerns today, there is a significant push towards developing and utilizing clean energy, especially renewable solar energy, to address these environmental issues.[120–129] Industrial activities contribute significantly to pollution, with approximately 800 000 tons of dyes produced globally yearly. These dyes persist in water due to their aromatic components and are highly toxic.[130,131] Therefore, effectively addressing dye contamination in water is crucial for ensuring safe public water supplies. Photocatalysis emerges as a highly effective and straightforward technique for treating dye pollutants and removing organic contaminants due to its complete degradation capabilities and broad applicability.[132–134] However, this method's effectiveness depends on the properties of the photocatalyst employed. Nanostructured semiconductors are emerging as auspicious materials for environmental remediation due to their ability to facilitate photocatalytic oxidation processes. When exposed to solar or UV light, these semiconductors can generate reactive species that degrade pollutants, effectively cleaning up environmental contaminants. The photocatalytic process can be broken down into three main steps. First, photocatalysts such as TiO_2 are activated by light energy that meets or exceeds the band gap energy, facilitating the generation of photoinduced charge carriers. Electrons in the valence band (VB) are excited to the conduction band (CB), leaving behind holes due to unoccupied electronic states (Scheme 4). Consequently, photoinduced electrons react with O_2 and H_2O to produce highly reactive superoxide and hydroxyl radicals. The O_2 adsorbed on the photocatalyst's surface captures electrons to form superoxide radicals ($\cdot O_2^-$). These superoxide radicals can further react with water to create hydroperoxyl radicals ($HO_2\cdot$). Additionally, water or hydroxide ions (OH^-) adsorbed on the photocatalyst's surface are oxidized by holes (h^+) to produce hydroxyl radicals ($\cdot OH$). Third, these highly reactive hydroperoxyl, hydroxyl, and superoxide radicals oxidize organic pollutants (OPs) into CO_2 and H_2O, thus avoiding secondary pollution.

5.3.1 MXene-modified QD heterostructures for photocatalytic pollutant degradation. The improved photocatalytic performance of a heterostructure is primarily due to effective electron transfer, reduced recombination, and enhanced light absorption and surface area. Following a hydrothermal strategy, a double heterojunction BPQDs/Ti_3C_2@TiO_2 photocatalyst was prepared, which promotes the fast electron transfer within the charge transport channels, resulting in considerable development in the degradation of methyl orange (MO) through the photocatalytic process, attributed to the significant specific surface area of the nanocomposite.[71] Furthermore, the enlarged specific surface area of BPQDs/Ti_3C_2@TiO_2 offers an increased density of surface-active sites and enhanced adsorption, significantly improving its photocatalytic performance of 93% methyl orange (MO) degradation in 60 minutes. These results highlight Ti_3C_2 MXene as a promising photocatalytic material and emphasize the critical contribution of BPQDs in photocatalytic degradation. Similarly, CdS quantum dots (QDs) have attracted attention in photocatalysis for their specific size-dependent electronic and optical properties, and based on these characteristics, the CdS QDs/$Ti_3C_2T_x$ exhibit remarkable photocatalytic activity in carbamazepine (CBZ) degradation, achieving efficiencies of 95.2%, 91.6%, and 91.7% in DI water, secondary effluent originating from municipal wastewater, and associated groundwater sources, respectively.

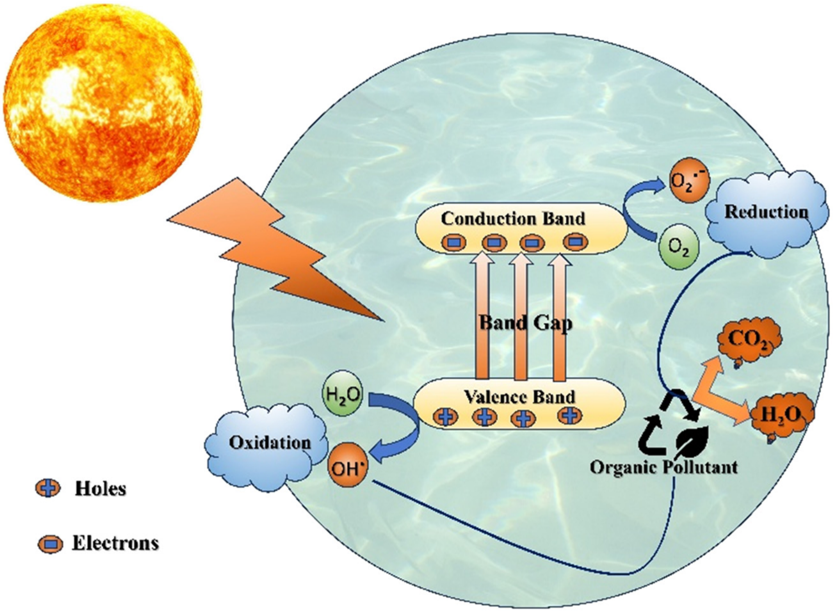

Scheme 4 Schematic representation of pollutant degradation.

The binary composite outperforms pure CdS in photocatalytic activity, with the optimal CT-9 (9 SILAR cycle) photocatalyst achieving high CBZ degradation efficiency under simulated sunlight. In addition, the suggested reaction mechanisms for CT-9-induced photocatalytic pollutant degradation are presented schematically in Fig. 12(a). Further, as shown in Fig. 12(b), several reactive oxygen species (ROS), particularly superoxide radicals ($\cdot O_2^-$), hydroxyl radicals ($\cdot OH$), and singlet oxygen ($^1O_2$), collectively contribute to CT-9-driven photocatalytic CBZ degradation under simulated sunlight, with $\cdot O_2^-$ playing the dominant role. Spin-trapping ESR analysis validated the generation of $\cdot O_2^-$, $\cdot OH$, and $^1O_2$ over CT-9 under simulated sunlight, supporting their key roles in the photocatalytic process as represented in Fig. 12(c). Similarly, Fig. 12(d) demonstrates the complete dye removal process of the CdS QDs@MXene/PVDF nanocomposite in detail. Additionally, carbon quantum dots (CQDs) have gathered significant interest in visible-light-driven heterogeneous photocatalysis due to their outstanding water solubility, efficient electron transport, and enhanced light-harvesting properties, which allow the complete utilization of the solar spectrum, leading to the development of CQDs/MXene heterostructures.[104] As depicted in Fig. 13, the nanocomposite demonstrated exceptional visible-light photocatalytic efficiency, maintaining excellent activity over three photodegradation cycles and achieving 96.1% malachite green dye (MG) dye degradation after 25 minutes of exposure. Again, this degradation kinetics follow a first-order reaction and a rate constant (k) of 0.1382 min^{-1}, as described by the Langmuir–Hinshelwood model. Further, Liu *et al.* found a nanocomposite, where the CdS quantum dots (QDs) with photocatalytic properties were integrated into MXene channels to create a CdS QDs@MXene/PVDF composite membrane, which demonstrated enhanced separation capability with PVDF polymer serving as the support layer.[102] The composite membrane effectively removed Congo red (CR) and Rhodamine B (Rh B) dyes, achieving impressive removal rates of 97.3% for CR and 98.5% for Rh B, through the combined action of membrane separation and photocatalysis. The CdS QDs imparted self-cleaning properties, exceptional permeability, and selectivity to the membrane, maintaining over 90% dye retention and a permeate flux of 388.0 L m^{-2} h^{-1} after five photocatalytic cycles, demonstrating excellent resistance to contamination. Therefore, incorporating uniform-sized CdS QDs within the interlayer channels of MXene enhanced the membrane's structure with photocatalytic and antifouling properties for stable and efficient dye removal from aqueous solutions. Table 1 summarizes the photocatalytic pollutant degradation of various MXene Ti_3C_2-modified QD nanocomposites under different experimental conditions.

The varying performance observed in different Ti_3C_2 MXene-modified quantum dot (QD) heterostructure catalysts can be primarily attributed to differences in interfacial

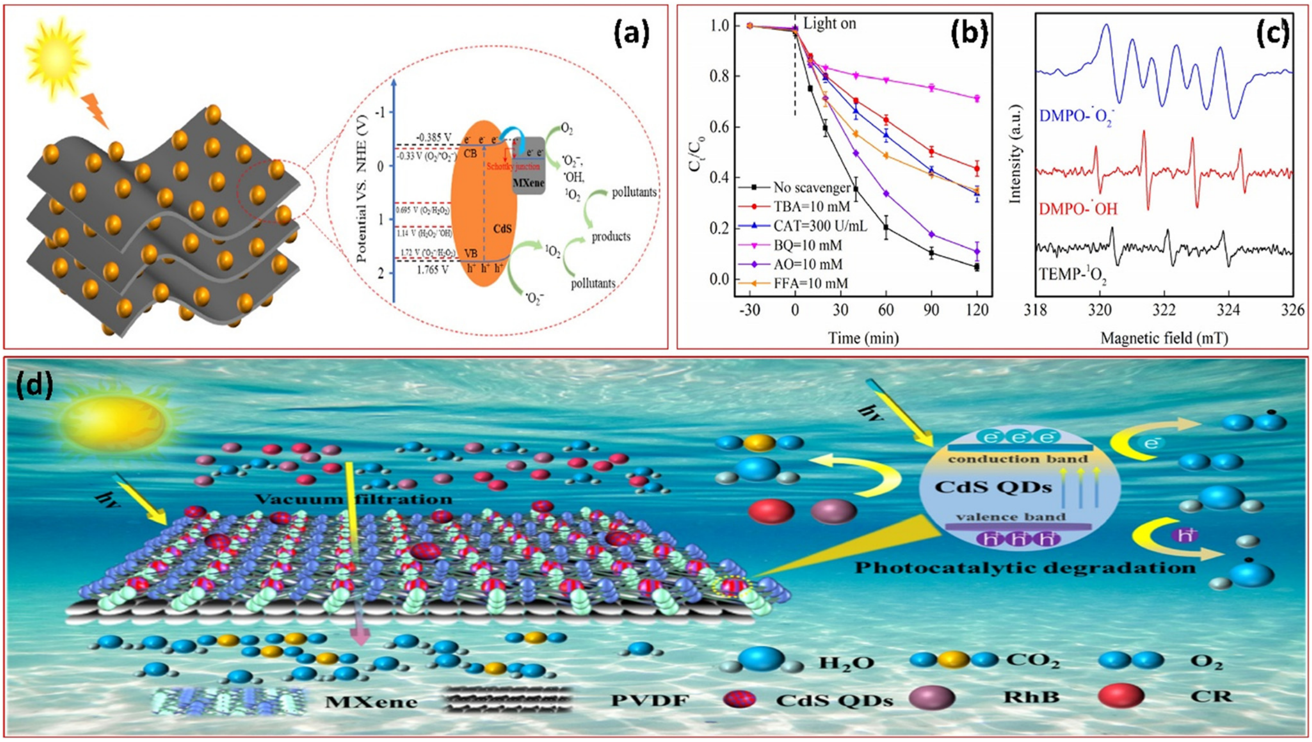

Fig. 12 (a) Proposed mechanism of CT-9 for the photodegradation of pollutants, (b) effect of various ROS scavengers on the degradation of CBZ by CT-9 and (c) ESR spectra of radical adducts trapped by DMPO or TEMP for CT-9, experimental conditions: [CBZ]0 = 10 mg L^{-1}, [CT-9] = 0.5 g L^{-1}, T = 25 °C. Reproduced from ref. 103 with permission from American Chemical Society, copyright 2023. (d) Diagram of the dye removal process of the CdS QDs@MXene/PVDF composite membrane. Reproduced from ref. 102 with permission from Elsevier, copyright 2024.

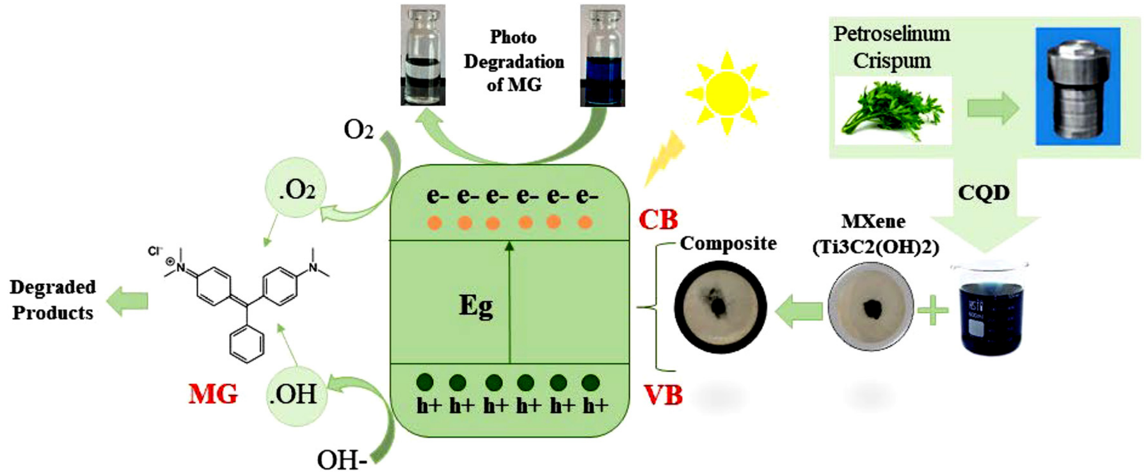

Fig. 13 An illustration of the photocatalytic pathway for MG degradation by the CQDs/MXene nanocomposite. Reproduced from ref. 104 with permission from Elsevier, copyright 2024.

interactions, electronic structure alignment, surface chemistry, and synthesis methods.[135–146] One of the most critical factors is the nature of the interface between the Ti_3C_2 MXene and the quantum dots. Strong interfacial coupling facilitates more efficient charge separation and transfer, which reduces electron–hole recombination and enhances overall catalytic activity. This efficiency is further influenced by the band alignment between the QDs and the MXene. A well-matched energy level configuration, particularly type-II band alignment, enables spatial separation of photoexcited electrons and holes, promoting higher photocatalytic or electrocatalytic performance. Additionally, the surface terminations on the MXene (*e.g.*, –OH, –F, or –O) play a significant role in determining its electronic structure, work function, and surface reactivity, all of which impact the overall behavior of the heterostructure. The composition and size of the quantum dots also influence performance through their effect on bandgap energy, light absorption, and quantum confinement effects. Smaller QDs tend to have more tunable band positions, which can enhance interfacial charge transfer if properly aligned with the MXene. Moreover, morphological factors such as the surface area and dispersion of QDs on the MXene surface determine the number of accessible active sites and the efficiency of mass and charge transport. Finally, the method used to fabricate the heterostructure whether through *in situ* growth, hydrothermal methods, or physical mixing affects interface quality, defect density, and material integration. Therefore, the performance differences across various MXene modified QD catalysts are a result of the complex interplay between these structural, electronic, and chemical factors, often tailored further by the specific requirements of the target catalytic or photocatalytic reaction.

Ti_3C_2 MXene-modified quantum dot (QD) heterostructures exhibit several fundamental similarities that enhance both energy conversion and environmental remediation processes. A key commonality is their ability to promote efficient charge separation and transfer, as the metallic conductivity of Ti_3C_2 MXene allows it to act as an electron sink, reducing charge recombination in quantum dots. This facilitates more effective photocatalytic reactions in pollutant degradation and boosts performance in solar energy conversion. Additionally, the combination of 2D MXene with 0D QDs results in a high surface area structure that increases active sites for redox reactions, enhancing both catalytic and adsorption capabilities. Their broad light absorption range, enabled by the tunable bandgap of QDs and the light-harvesting properties of MXenes, further supports efficient utilization of solar energy. Moreover, favorable band alignment between QDs and MXene supports synergistic charge transfer mechanisms like type-II or Z-scheme systems, improving redox activity for both environmental and energy applications. Lastly, the chemical stability and surface functionality of Ti_3C_2 facilitate strong interfacial interactions with QDs, contributing to the structural integrity and operational durability of the heterostructure across diverse applications. Ti_3C_2 MXene-modified quantum dot (QD) heterostructures, while sharing several similarities, also exhibit considerable differences in their formation and function depending on whether they are applied to energy conversion or environmental remediation. In energy conversion systems, such as solar cells, the heterostructures are often designed with precise band alignment and charge transfer dynamics in mind, requiring careful control over QD size, composition, and interface engineering to optimize light absorption. In contrast, environmental remediation applications, like pollutant degradation, typically prioritize surface reactivity, adsorption capacity, and catalytic efficiency over long-term charge transport optimization. Additionally, the synthesis strategies may differ: for energy applications, more sophisticated methods (*e.g.*, epitaxial growth or atomic layer deposition) are employed to ensure structural coherence and stability, whereas for remediation, simpler, scalable approaches (like hydrothermal synthesis or *in situ* deposition) are favored for cost-effectiveness. The choice of QD material also varies; semiconducting QDs with optimal band gaps are selected for solar energy harvesting, while QDs with higher surface catalytic activity or redox potential (such as doped or defect-rich QDs) are more commonly used in pollutant breakdown. These distinctions in heterostructure design reflect the differing performance demands of energy *versus* environmental systems, even though both benefit from the unique properties of the Ti_3C_2 MXene–QD hybrid framework.

5.4. Role of MXene and quantum dots in different photocatalytic applications

MXenes and quantum dots (QDs) have distinct roles in photocatalytic systems. Ti_3C_2 MXene often acts as a conductive support, electron mediator, or co-catalyst, enhancing charge transport, reducing electron–hole recombination, and sometimes providing active sites. It can also serve as an electron sink, promoting efficient charge separation and utilization.

QDs play versatile roles in photocatalysis as semiconductors, co-catalysts, and sensitizers especially when paired with MXenes. These synergistic composites offer enhanced light harvesting, charge transport, and stability, making them promising candidates for energy conversion and environmental remediation applications.

Role of quantum dots

1. QDs as semiconductors. Quantum dots enhance photocatalytic activity by improving light absorption, charge separation, and electron mobility when integrated with materials like MXenes. Studies demonstrate that such hybrids significantly outperform their individual components. For example, BPQDs/Ti_3C_2@TiO_2 and CdS QDs/$Ti_3C_2T_x$ showed superior performance in hydrogen evolution, pollutant degradation, and CO_2 reduction, primarily due to improved heterojunction formation, larger surface areas, and more efficient charge transfer.

2. QDs as co-catalysts. QDs also act as co-catalysts, enhancing reaction efficiency by accelerating charge separation, reducing over potential, and stabilizing photocatalysts. For example, when Pt QDs combined with TiO_2 nanowires and Ti_3C_2 MXene, a 16.58-fold increase in CO_2 reduction compared to commercial TiO_2 is achieved. However, excessive QD loading can hinder performance by blocking light and active sites or promoting charge recombination.

3. QDs as sensitizers. As sensitizers, QDs absorb visible light and generate charge carriers, which are transferred to MXenes to drive photocatalytic reactions. For instance, CdSe QDs coupled with $Ti_3C_2T_x$ MXene significantly improved hydrogen production and pollutant reduction due to strong interfacial contact and efficient electron extraction. Optimal MXene loading is critical, as excessive amounts can reduce light absorption by QDs.

6. Outlook and future perspective

In conclusion, this review highlights advancements in the design and development of MXene-modified QD composites for exceptional photocatalytic applications, such as H_2 evolution, CO_2 reduction, and pollutant detoxification, while also discussing the fundamental principles and scalability of these processes. It covers various synthesis methods and the characteristics of MXene-modified QD nanocomposites. Due to their 2D morphology, layered structures, and flexibility, MXenes are ideal candidates for multifunctional composites, sparking increased interest in MXene-modified materials. Despite the photocatalytic potential of QDs, issues like charge recombination and instability persist, but MXenes address these challenges, making MXene-modified QD composites highly promising for energy conservation and environmental applications. The combined effort between MXenes and QDs enhances interfacial interactions, electronic coupling, and improves conductivity, optical properties, and stability. These composites have shown improved hydrogen generation, CO_2 reduction with higher fuel yield and selectivity, and effective photocatalysis for wastewater treatment. While significant progress has been made, challenges remain in large-scale fabrication, long-term stability, and optimizing interfacial properties for maximum efficiency. Future research should focus on cost-effective, scalable synthesis methods, novel MXene–QD combinations, and a deeper understanding of charge transfer dynamics to enable the practical implementation of MXene-modified QDs in next-generation energy conversion and environmental remediation technologies. The different aspects of future prospects and outlooks are represented in Scheme 5. To achieve faster progress in this area, it is crucial to concentrate on the following key areas:

1. **Exploring the synergistic effects of active metals in MXene-modified QD composites:** future research should focus on synthesizing various binary and ternary MXene materials incorporating metals such as Ni, V, Cu, Cd, Ce, and Mn. These materials can be integrated with different quantum dots, such as CdSe, PbS, and perovskite QDs, as well as other functional nanomaterials like fullerenes, selenium compounds, tellurides, and noble metals (*e.g.*, Pt, Au, Ag). This approach is expected to significantly improve energy conversion efficiency in photocatalysis and expand its functional applications.

2. **Developing nanohybrids through innovative synthetic methods:** there is a significant demand for scalable synthesis approaches to create MXene-modified QD composite catalysts, including mechanical mixing/self-assembly, *in situ* decoration, and *in situ* oxidation techniques. This will facilitate the systematic advancement of improved MXene-modified QD catalysts. Therefore, it is crucial to focus on the large-scale preparation of efficient and durable MXene-modified QD composite catalysts using various methods in the coming years.

3. **Functionality modification:** altering MXene by introducing defects, doping, and diversifying the nanostructured morphology can address the limitations of MXene and improve the catalytic performance of MXene-modified QD composites. Carefully controlling

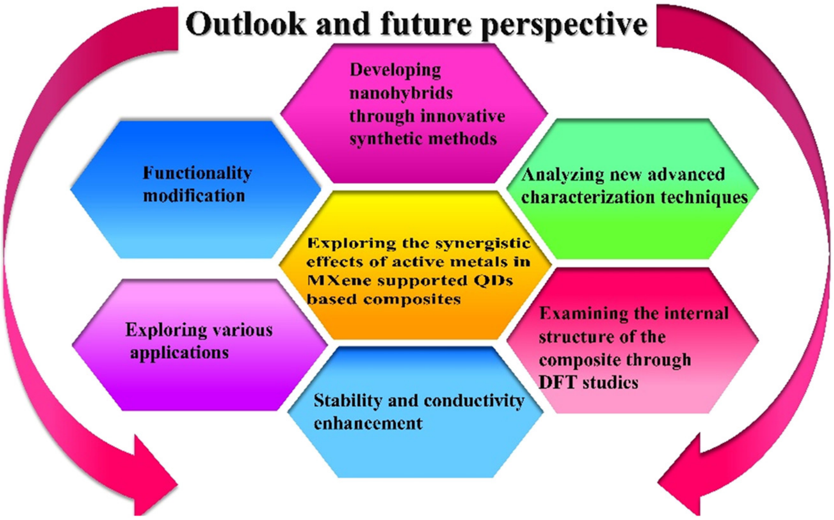

Scheme 5 Different directions of outlook and future perspective.

the ratio of MXene to QDs during the preparation process can enhance conductivity, boost activity, and enable the formation of smaller, well-dispersed hybrid materials.

4. **Analyzing new advanced analytical techniques:** to explore the physicochemical properties of hybrid materials, various advanced characterization methods such as scanning probe microscopy (SPM), near-field scanning optical microscopy (NSOM), and magnetic resonance force microscopy (MRFM) should be employed. These techniques provide valuable insights into the changes in interfacial, chemical, and electronic properties within these hybrid structures.

5. **Examining the internal structure of the composite through DFT studies:** understanding the unique characteristics of MXene is vital for different photocatalytic applications, making it essential to investigate the underlying mechanisms. Conducting theoretical modeling of MXene-modified QD composites is particularly important, as it offers valuable insights into electron distribution within the MXene and the QD structure. By integrating simulation results with experimental findings, we can deepen our understanding of the photocatalytic processes involved. A thorough examination of the internal structure, morphology, crystallinity, conductivity, and stability of MXene-supported QDs is crucial, as increased interlayer spacing may lead to structural instability, volume expansion, and related issues that can ultimately affect photocatalytic performance. Therefore, DFT studies are highly valuable in this context.

6. **Exploring various applications:** the mechanisms, reaction pathways, and product selectivity in the photocatalytic reduction of N_2 to NH_3 and the production of H_2O_2 using MXene-modified QDs are still not well understood. Therefore, it is crucial to conduct a comprehensive investigation to enhance our understanding of photogenerated charge transfer dynamics during these photocatalytic processes involving MXene-modified QD hybrids. Achieving large-scale applications and commercial viability for MXene-based materials with cost-effective modifications remains a significant challenge for future research.

7. **Stability and conductivity enhancement:** improving the recyclability of hybrid catalysts is essential for their sustainable and commercial use. Strengthening the internal interactions between MXene and QDs can improve the overall stability of the materials. Additionally, chemical modifications of the composite materials can further boost their conductivity. Various aspects of future prospects are illustrated in Scheme 5. However, MXene modified heterostructures are still in the preliminary stages of fundamental research and require significant advancements before realizing their full scientific and technological potential.

Conflicts of interest

There are no conflicts to declare.

Data availability

No primary research results, software or code have been included and no new data were generated or analysed as part of this review.

Acknowledgements

The authors gratefully acknowledge the support and encouragement provided by the management of S 'O' A (Deemed to be University), Bhubaneswar.

References

1 T. Kong, Y. Jiang and Y. Xiong, *Chem. Soc. Rev.*, 2020, **49**, 6579–6591.

2 Z. Kovacic, B. Likozar and M. Hus, *ACS Catal.*, 2020, **10**, 14984–15007.

3 G. Murali, S. P. Vattikuti, Y. K. Kshetri, H. Lee, J. K. R. Modigunta, C. S. Reddy, S. Park, S. Lee, B. Poornaprakash, H. Lee and Y. H. Park, *Chem. Eng. J.*, 2021, **421**, 12968.

4 D. Chen, Y. Cheng, N. Zhou, P. Chen, Y. Wang, K. Li, S. Huo, P. Cheng, P. Peng, R. Zhang and L. Wang, *J. Cleaner Prod.*, 2020, **268**, 121725.

5 N. Fajrina and M. Tahir, *Int. J. Hydrogen Energy*, 2019, **44**, 540–577.

6 X. Chang, T. Wang and J. Gong, *Energy Environ. Sci.*, 2016, **9**, 2177–2196.

7 A. Nawaz, A. Kuila, N. S. Mishra, K. H. Leong, L. C. Sim, P. Saravanan and M. Jang, *Rev. Chem. Eng.*, 2021, **37**, 533–560.

8 X. Wang, F. Wang, Y. Sang and H. Liu, *Adv. Energy Mater.*, 2017, **7**, 1700473.

9 K. Rajeshwar, N. R. de Tacconi and C. R. Chenthamarakshan, *Chem. Mater.*, 2001, **13**, 2765–2782.

10 H. Tong, S. Ouyang, Y. Bi, N. Umezawa, M. Oshikiri and J. Ye, *Adv. Mater.*, 2012, **24**, 229–251.

11 B. Seo, G. Y. Jung, Y. J. Sa, H. Y. Jeong, J. Y. Cheon, J. H. Lee, H. Y. Kim, J. C. Kim, H. S. Shin, S. K. Kwak and S. H. Joo, *ACS Nano*, 2015, **9**, 3728–3739.

12 B. Zhao, J. Song, P. Liu, W. Xu, T. Fang, Z. Jiao, H. Zhang and Y. Jiang, *J. Mater. Chem.*, 2011, **21**, 18792–18798.

13 C. Zhang, J. Zhao, L. Zhou, Z. Li, M. Shao and M. Wei, *J. Mater. Chem. A*, 2016, **4**, 11516–11523.

14 M. Wang, L. Cai, Y. Wang, F. Zhou, K. Xu, X. Tao and Y. Chai, *J. Am. Chem. Soc.*, 2017, **139**, 4144–4151.

15 Y. Zhu, J. Ren, G. Huang, C. L. Dong, Y. C. Huang, P. Lu, H. Tang, Y. Liu, S. Shen and D. Yang, *Adv. Funct. Mater.*, 2024, **9**, 2311623.

16 Q. Zhang, S. Huang, J. Deng, D. T. Gangadharan, F. Yang, Z. Xu, G. Giorgi, M. Palummo, M. Chaker and D. Ma, *Adv. Funct. Mater.*, 2019, **29**, 1902486.

17 B. Anasori, M. R. Lukatskaya and Y. Gogotsi, *2D metal carbides and nitrides (MXenes) for energy storage*, Jenny Stanford Publishing, 2023, pp. 677–722.

18 M. Naguib, M. Kurtoglu, V. Presser, J. Lu, J. Niu, M. Heon, L. Hultman, Y. Gogotsi and M. W. Barsoum, *Two-dimensional nanocrystals produced by exfoliation of Ti_3AlC_2*, Jenny Stanford Publishing, 2023, pp. 15–29.

19 M. Naguib, O. Mashtalir, J. Carle, V. Presser, J. Lu, L. Hultman, Y. Gogotsi and M. W. Barsoum, *ACS Nano*, 2012, **6**, 1322–1331.

20 M. Ghidiu, M. Naguib, C. Shi, O. Mashtalir, L. M. Pan, B. Zhang, J. Yang, Y. Gogotsi, S. J. Billinge and M. W. Barsoum, *Chem. Commun.*, 2014, **50**, 9517–9520.

21 M. Naguib, V. N. Mochalin, M. W. Barsoum and Y. Gogotsi, *Adv. Mater.*, 2014, **26**, 992–1005.

22 P. Priyadarshini and K. Parida, *J. Energy Storage*, 2024, **87**, 111379.

23 S. Das, G. Swain and K. Parida, *Sustainable Energy Fuels*, 2022, **6**, 937–953.

24 D. Kandi, S. Martha and K. M. Parida, *Int. J. Hydrogen Energy*, 2017, 9467–9481.

25 U. A. Mohanty, D. P. Sahoo, L. Paramanik and K. Parida, *Sustainable Energy Fuels*, 2023, **7**, 1145–1186.

26 D. P. Sahoo, K. K. Das, S. Mansingh, S. Sultana and K. Parida, *Coord. Chem. Rev.*, 2022, **469**, 214666.

27 A. Mishra, N. Priyadarshini, S. Mansingh and K. Parida, *Adv. Colloid Interface Sci.*, 2024, 103300.

28 L. Biswal, R. Mohanty, S. Nayak and K. Parida, *J. Environ. Chem. Eng.*, 2022, **10**, 107211.

29 L. Biswal, S. Nayak and K. Parida, *Catal. Sci. Technol.*, 2021, **11**, 1222–1248.

30 J. Sahu, D. Prusty, S. Mansingh and K. Parida, *Int. J. Hydrogen Energy*, 2023, **48**, 29097–29118.

31 M. Khazaei, M. Arai, T. Sasaki, C. Y. Chung, N. S. Venkataramanan, M. Estili, Y. Sakka and Y. Kawazoe, *Adv. Funct. Mater.*, 2013, **23**, 2185–2192.

32 M. Naguib, M. Kurtoglu, V. Presser, J. Lu, J. Niu, M. Heon, L. Hultman, Y. Gogotsi and M. W. Barsoum, *Two-dimensional nanocrystals produced by exfoliation of Ti_3AlC_2*, Jenny Stanford Publishing, 2023, pp. 15–29.

33 P. Simon, *ACS Nano*, 2017, **11**, 2393–2396.

34 H. Fang, Y. Pan, M. Yin, L. Xu, Y. Zhu and C. Pan, *J. Solid State Chem.*, 2019, **280**, 120981.

35 X. Jiang, A. V. Kuklin, A. Baev, Y. Ge, H. Ågren, H. Zhang and P. N. Prasad, *Phys. Rep.*, 2020, **848**, 1–58.

36 X. Zhang, Z. Zhang, J. Li, X. Zhao, D. Wu and Z. Zhou, *J. Mater. Chem. A*, 2017, **5**, 12899–12903.

37 X. D. Zhu, Y. Xie and Y. T. Liu, *J. Mater. Chem. A*, 2018, **6**, 21255–21260.

38 Q. Liu, L. Ai and J. Jiang, *J. Mater. Chem. A*, 2018, **6**, 4102–4110.

39 B. Anasori, Y. Xie, M. Beidaghi, J. Lu, B. C. Hosler, L. Hultman, P. R. C. Kent, Y. Gogotsi and M. W. Barsoum, *ACS Nano*, 2015, **9**, 9507–9516.

40 N. R. Hemanth, T. Kim, B. Kim, A. H. Jadhav, K. Lee and N. K. Chaudhari, *Mater. Chem. Front.*, 2021, **5**, 3298–3321.

41 N. C. Frey, J. Wang, G. I. Vega Bellido, B. Anasori, Y. Gogotsi and V. B. Shenoy, *ACS Nano*, 2019, **13**, 3031–3041.

42 J. Pan, S. Lany and Y. Qi, *ACS Nano*, 2017, **11**, 7560–7564.

43 J. Ran, G. Gao, F. T. Li, T. Y. Ma, A. Du and S. Z. Qiao, *Nat. Commun.*, 2017, **8**, 13907.

44 S. Zhao, D. Pan, Q. Liang, M. Zhou, C. Yao, S. Xu and Z. Li, *J. Phys. Chem. C*, 2021, **125**, 10207–10218.

45 P. Sun, Z. Xing, Z. Li and W. Zhou, *Chem. Eng. J.*, 2023, **458**, 141399.

46 M. Guo, Z. Xing, T. Zhao, Z. Li, S. Yang and W. Zhou, *Appl. Catal., B*, 2019, **257**, 117913.

47 J. Sahu, S. Mansingh, B. P. Mishra, D. Prusty and K. Parida, *Dalton Trans.*, 2023, **52**, 16525–16537.

48 M. Faraji, M. Yousefi, S. Yousefzadeh, M. Zirak, N. Naseri, T. H. Jeon, W. Choi and A. Z. Moshfegh, *Energy Environ. Sci.*, 2019, **12**, 59–95.

49 Y. Yan, J. Gong, J. Chen, Z. Zeng, W. Huang, K. Pu, J. Liu and P. Chen, *Adv. Mater.*, 2019, **31**, 1808283.

50 J. Yang, T. Ling, W. T. Wu, H. Liu, M. R. Gao, C. Ling, L. Li and X. W. Du, *Nat. Commun.*, 2013, **4**, 1695.

51 X. Chen, Q. Liu, Q. Wu, P. Du, J. Zhu, S. Dai and S. Yang, *Adv. Funct. Mater.*, 2016, **26**, 1719–1728.

52 G. Wang, H. Ni, Y. Li, H. Torun, S. Chen, M. W. Shahzad, X. Zhang, S. Y. Zheng, B. B. Xu and J. Yang, *Adv. Funct. Mater.*, 2025, 2505048.

53 M. Alhabeb, K. Maleski, B. Anasori, P. Lelyukh, L. Clark, S. Sin and Y. Gogotsi, *Chem. Mater.*, 2017, **29**, 7633–7644.

54 R. M. Ronchi, J. T. Arantes and S. F. Santos, *Ceram. Int.*, 2019, **45**, 18167–18188.

55 L. Biswal, L. Acharya, B. P. Mishra, S. Das, G. Swain and K. Parida, *ACS Appl. Energy Mater.*, 2023, **6**, 2081–2096.

56 Q. Tang, Z. Zhou and P. Shen, *J. Am. Chem. Soc.*, 2012, **134**, 16909–16916.

57 M. Naguib, M. Kurtoglu, V. Presser, J. Lu, J. Niu, M. Heon, L. Hultman, Y. Gogotsi and M. W. Barsoum, *Two-dimensional nanocrystals produced by exfoliation of Ti_3AlC_2*, Jenny Stanford Publishing, 2023, pp. 15–29.

58 J. Ran, G. Gao, F. T. Li, T. Y. Ma, A. Du and S. Z. Qiao, *Nat. Commun.*, 2017, **8**, 13907.

59 H. W. Wang, M. Naguib, K. Page, D. J. Wesolowski and Y. Gogotsi, *Chem. Mater.*, 2016, **28**, 349–359.

60 M. A. Hope, A. C. Forse, K. J. Griffith, M. R. Lukatskaya, M. Ghidiu, Y. Gogotsi and C. P. Grey, *Phys. Chem. Chem. Phys.*, 2016, **18**, 5099–5102.

61 B. Anasori, M. R. Lukatskaya and Y. Gogotsi, *2D metal carbides and nitrides (MXenes) for energy storage*, Jenny Stanford Publishing, 2023, pp. 677–722.

62 M. A. Hope, A. C. Forse, K. J. Griffith, M. R. Lukatskaya, M. Ghidiu, Y. Gogotsi and C. P. Grey, *Phys. Chem. Chem. Phys.*, 2016, **18**, 5099–5102.

63 C. A. Voigt, M. Ghidiu, V. Natu and M. W. Barsoum, *J. Phys. Chem. C*, 2018, **122**, 23172–23179.

64 J. Halim, K. M. Cook, M. Naguib, P. Eklund, Y. Gogotsi, J. Rosen and M. W. Barsoum, *Appl. Surf. Sci.*, 2016, **362**, 406–417.

65 M. Naguib, R. R. Unocic, B. L. Armstrong and J. Nanda, *Dalton Trans.*, 2015, **44**, 9353–9358.

66 I. Persson, L.-Å. Näslund, J. Halim, M. W. Barsoum, V. Darakchieva, J. Palisaitis, J. Rosen and P. O. Å. Persson, *2D Mater.*, 2017, **5**, 015002.

67 P. Lian, Y. Dong, Z. S. Wu, S. Zheng, X. Wang, S. Wang, C. Sun, J. Qin, X. Shi and X. Bao, *Nano Energy*, 2017, **40**, 1–8.

68 X. Li, Y. Bai, X. Shi, N. Su, G. Nie, R. Zhang, H. Nie and L. Ye, *Mater. Adv.*, 2021, **2**, 1570–1594.

69 Y. Li, L. Ding, Z. Liang, Y. Xue, H. Cui and J. Tian, *Chem. Eng. J.*, 2020, **383**, 123178.

70 Y. Li, S. Yang, Z. Liang, Y. Xue, H. Cui and J. Tian, *Mater. Chem. Front.*, 2019, **3**, 2673–2680.

71 M. Seredych, C. E. Shuck, D. Pinto, M. Alphabet, E. Precetti, G. Deysher, B. Anasori, N. Kurra and Y. Gogotsi, *Chem. Mater.*, 2019, **31**, 3324–3332.

72 S. C. Zhu, S. Li, B. Tang, H. Liang, B. J. Liu, G. Xiao and F. X. Xiao, *J. Catal.*, 2021, **404**, 56–66.

73 W. Li, C. Zhuang, Y. Li, C. Gao, W. Jiang, Z. Sun and K. Qi, *Ceram. Int.*, 2021, **47**, 21769–21776.

74 S. N. Baker and G. a. Baker, *Angew. Chem., Int. Ed.*, 2010, **49**, 6726–6744.

75 Y. Zhao, Y. Chen, Y. H. Zhang and S. F. Liu, *Mater. Chem. Phys.*, 2017, **189**, 215–229.

76 R. Zhang, X. Y. Zhou, D. Zhang, W. K. Lou, F. Zhai and K. Chang, *2D Mater.*, 2015, **2**, 045012.

77 Z. Yao, H. Sun, H. Sui and X. Liu, *Nanomaterials*, 2020, **10**, 452.

78 J. Low, L. Zhang, T. Tong, B. Shen and J. Yu, *J. Catal.*, 2018, **361**, 255–266.

79 T. Song, L. Hou, B. Long, A. Ali and G. J. Deng, *J. Colloid Interface Sci.*, 2021, **584**, 474–483.

80 P. Zhou, F. Lv, N. Li, Y. Zhang, Z. Mu, Y. Tang, J. Lai, Y. Chao, M. Luo, F. Lin and J. Zhou, *Nano Energy*, 2019, **56**, 127–137.

81 Z. Qin, C. Ouyang, J. Zhang, L. Wan, S. Wang, C. Xie and D. Zeng, *Sens. Actuators, B*, 2017, **253**, 1034–1042.

82 A. Thibert, F. A. Frame, E. Busby, M. A. Holmes, F. E. Osterloh and D. S. Larsen, *J. Phys. Chem. Lett.*, 2011, **2**, 2688–2694.

83 Y. Xie, G. Ali, S. H. Yoo and S. O. Cho, *ACS Appl. Mater. Interfaces*, 2010, **2**, 2910–2914.

84 J. Shen, J. Shen, W. Zhang, X. Yu, H. Tang, M. Zhang and Q. Liu, *Ceram. Int.*, 2019, **45**, 4146–24153.

85 L. Zhang, J. Yang, T. Xie, S. Feng and L. Xu, *Mater. Des.*, 2020, **192**, 108772.

86 X. Feng, Z. Yu, Y. Sun, M. Shan, R. Long and X. Li, *Sep. Purif. Technol.*, 2021, **266**, 118606.

87 G. Nedelcu, L. Protesescu, S. Yakunin, M. I. Bodnarchuk, M. J. Grotevent and M. V. Kovalenko, *Nano Lett.*, 2015, **15**, 5635–5640.

88 N. Wang, L. Cheng, R. Ge, S. Zhang, Y. Miao, W. Zou, C. Yi, Y. Sun, Y. Cao, R. Yang and Y. Wei, *Nat. Photonics*, 2016, **10**, 699–704.

89 W. S. Yang, B. W. Park, E. H. Jung, N. J. Jeon, Y. C. Kim, D. U. Lee, S. S. Shin, J. Seo, E. K. Kim, J. H. Noh and S. I. Seok, *Science*, 2017, **356**, 1376–1379.

90 S. Shyamal and N. Pradhan, *J. Phys. Chem. Lett.*, 2020, **11**, 6921–6934.

91 Y. Zhang, W. Chen, M. Zhou, G. Miao and Y. Liu, *ACS Appl. Energy Mater.*, 2021, **4**, 9154–9165.

92 M. Que, Y. Zhao, Y. Yang, L. Pan, W. Lei, W. Cai, H. Yuan, J. Chen and G. Zhu, *ACS Appl. Mater. Interfaces*, 2021, **13**, 6180–6187.

93 M. Que, Y. Zhao, L. Pan, Y. Yang, Z. He, H. Yuan, J. Chen and G. Zhu, *Mater. Lett.*, 2021, **282**, 128695.

94 J. Wang, J. Wang, N. Li, X. Du, J. Ma, C. He and Z. Li, *ACS Appl. Mater. Interfaces*, 2020, **12**, 31477–31485.

95 B. Li, C. Lai, G. Zeng, D. Huang, L. Qin, M. Zhang, M. Cheng, X. Liu, H. Yi, C. Zhou and F. Huang, *Small*, 2019, **8**, 1804565.

96 K. C. Devarayapalli, S. P. Vattikuti, D. J. Kim, Y. Lim, B. Kim, G. Kim and D. S. Lee, *J. Energy Chem.*, 2023, **82**, 27–637.

97 Z. Raad, J. Toufaily, T. Hamieh and M. E. Domine, *Nanomater.*, 2021, **9**, 2380.

98 C. Peng, X. Yang, Y. Li, H. Yu, H. Wang and F. Peng, *ACS Appl. Mater. Interfaces*, 2016, **8**, 6051–6060.

99 T. Y. Ma, J. L. Cao, M. Jaroniec and S. Z. Qiao, *Angew. Chem., Int. Ed.*, 2016, **55**, 1138–1142.

100 D. M. Almendinger, V. M. Engh, E. A. Strømsodd, H. E. Hansen, A. F. Buene, B. H. Hoff and O. R. Gautun, *ACS Omega*, 2022, **7**, 22046–22057.

101 J. Xu, Y. Chen, Z. Dong, Q. Wang, Y. Situ and H. Huang, *J. Mater. Sci.*, 2018, **53**, 12770–12780.

102 K. Liu, Y. Liu, Z. Cui, J. Zhang, X. Chen, X. Zheng, M. Xin, X. Zhang, Y. H. Chiao, A. Sengupta and G. Zeng, *J. Environ. Chem. Eng.*, 2024, **12**, 113813.

103 Z. Yang and J. Wang, *Langmuir*, 2023, **39**, 4179–4189.

104 M. M. Zahedi, S. K. Samarin, S. D. Abkenar, A. B. Pebdeni, M. Hosseini, S. Kalikeri and H. Karimi-Maleh, *J. Taiwan Inst. Chem. Eng.*, 2025, **166**, 105521.

105 A. Fujishima and K. Honda, *Nature*, 1972, **238**, 37–38.

106 Y. Xue, Y. Xie, C. Xu, H. He, Q. Jiang, G. Ying and H. Huang, *Surf. Interfaces*, 2022, **30**, 101917.

107 S. Y. Pang, W. F. Io and J. Hao, *Adv. Sci.*, 2021, **8**, 2102217.

108 M. Halmann, *Nature*, 1978, **275**, 115–116.

109 A. Lais, M. A. Gondal and M. A. Dastageer, *Environ. Chem. Lett.*, 2018, **16**, 183–210.

110 C. Wang, Z. Sun, Y. Zheng and Y. H. Hu, *J. Mater. Chem.*, 2019, **7**, 865–887.

111 H. Cho, W. D. Kim, K. Lee, S. Lee, G. S. Kang, H. I. Joh and D. C. Lee, *Appl. Surf. Sci.*, 2018, **429**, 2–8.

112 H. Cui, Y. Guo, L. Guo, L. Wang, Z. Zhou and Z. Peng, *Adv. Energy Mater.*, 2018, **6**, 18782–18793.

113 S. Cheng, Z. Sun, K. H. Lim, T. Z. H. Gani, T. Zhang, Y. Wang, H. Yin, K. Liu, H. Guo, T. Du and L. Liu, *Adv. Energy Mater.*, 2022, **12**, 2200389.

114 S. Du, Z. Ren, Y. Qu, J. Wu, W. Xi, J. Zhu and H. Fu, *Chem. Commun.*, 2016, **52**, 6705–6708.

115 M. R. Lukatskaya, O. Mashtalir, C. E. Ren, Y. Dall'Agnese, P. Rozier, P. L. Taberna, M. Naguib, P. Simon, M. W. Barsoum and Y. Gogotsi, *Science*, 2013, **341**, 1502–1505.

116 Y. Wen, T. E. Rufford, X. Chen, N. Li, M. Lyu, L. Dai and L. Wang, *Nano Energy*, 2017, **38**, 368–376.

117 X. Li, M. Zhan, Y. Liu, W. Tu and H. Li, *Chem. – Eur. J.*, 2024, **30**, e202400874.

118 Q. Tang, T. Li, W. Tu, H. Wang, Y. Zhou and Z. Zou, *Adv. Funct. Mater.*, 2024, **34**, 2311609.

119 K. M. Zhang and Z. G. Wen, *J. Environ. Manage.*, 2008, **88**, 1249–1261.

120 Y. Guo, Y. Ao, P. Wang and C. Wang, *Appl. Catal., B*, 2019, **254**, 479–490.

121 P. Cheera, S. Karlapudi, G. Sellola and V. Ponneri, *J. Mol. Liq.*, 2016, **221**, 993–998.

122 C. Prasad, G. Yuvaraja and P. Venkateswarlu, *J. Magn. Magn. Mater.*, 2017, **424**, 376–381.

123 C. Prasad, S. Karlapudi, P. Venkateswarlu, I. Bahadur and S. Kumar, *J. Mol. Liq.*, 2017, **240**, 22–328.

124 C. Prasad, S. Karlapudi, C. N. Rao, P. Venkateswarlu and I. Bahadur, *J. Mol. Liq.*, 2017, **243**, 611–615.

125 C. Prasad, P. K. Murthy, R. H. Krishna, R. S. Rao, V. Suneetha and P. Venkateswarlu, *J. Environ. Chem. Eng.*, 2017, **5**, 4374–4380.

126 D. P. Sahoo, S. Patnaik, D. Ratha and K. M. Parida, *Inorg. Chem. Front.*, 2018, **5**, 879–896.

127 S. Venkateswarlu, B. N. Kumar, C. H. Prasad, P. Venkateswarlu and N. V. V. Jyothi, *Phys. B*, 2014, **449**, 67–71.

128 C. Prasad, H. Tang and W. Liu, *J. Nanostruct. Chem.*, 2018, **8**, 393–412.

129 G. K. Naik, P. M. Mishra and K. Parida, *Chem. Eng. J.*, 2013, **229**, 492–497.

130 P. Kaur, V. K. Sangal and J. P. Kushwaha, *Int. J. Environ. Sci. Technol.*, 2019, **16**, 801–810.

131 W. Lemlikchi, S. Khaldi, M. O. Mecherri, H. Lounici and N. Drouiche, *Sep. Sci. Technol.*, 2012, **47**, 1682–1688.

132 Z. Lu, J. Peng, M. Song, Y. Liu, X. Liu, P. Huo, H. Dong, S. Yuan, Z. Ma and S. Han, *Chem. Eng. J.*, 2019, **360**, 1262–1276.

133 Y. Xue, P. Wang, C. Wang and Y. Ao, *Chemosphere*, 2018, **203**, 497–505.

134 G. Murali, J. K. Modigunta Reddy, Y. H. Park, J. H. Lee, J. Rawal, S. Y. Lee, I. In and S. J. Park, *ACS Nano*, 2022, **16**, 13370–13429.

135 S. De, S. Acharya, S. Sahoo, J. J. Shim and G. C. Nayak, *Mater. Chem. Front.*, 2022, **6**, 818–842.

136 K. Zhang, D. Li, H. Cao, Q. Zhu, C. Trapalis, P. Zhu, X. Gao and C. Wang, *Chem. Eng. J.*, 2021, **424**, 130340.

137 C. Prasad, X. Yang, Q. Liu, H. Tang, A. Rammohan, S. Zulfiqar, G. V. Zyryanov and S. Shah, *J. Ind. Eng. Chem.*, 2020, **85**, 1–33.

138 L. Cheng, X. Li, H. Zhang and Q. Xiang, *J. Phys. Chem. Lett.*, 2019, **10**, 3488–3494.

139 P. Prabha Sarangi, D. Prava Sahoo, U. Aparajita Mohanty, S. Nayak and K. Parida, *ChemCatChem*, 2024, **16**, 202301533.

140 C. Peng, T. Zhou, P. Wei, W. Xu, H. Pan, F. Peng, J. Jia, K. Zhang and H. Yu, *APL Mater.*, 2021, **9**, 070703.

141 F. Jamil, H. M. Ali and M. M. Janjua, *J. Energy Storage*, 2021, **35**, 102322.

142 A. Sherryna and M. Tahir, *ACS Appl. Energy Mater.*, 2021, **4**, 11982–12006.

143 X. Zhang, H. Xie, Z. Liu, C. Tan, Z. Luo, H. Li, J. Lin, L. Sun, W. Chen, Z. Xu and L. Xie, *Angew. Chem., Int. Ed.*, 2015, **54**, 3653–3657.

144 R. Gui, H. Jin, Z. Wang and J. Li, *Chem. Soc. Rev.*, 2018, **47**, 6795–6823.

145 W. Zhao, Z. Chen, X. Yang, X. Qian, C. Liu, D. Zhou, T. Sun, M. Zhang, G. Wei, P. D. Dissanayake and Y. S. Ok, *Renewable Sustainable Energy Rev.*, 2020, **132**, 110040.

146 Y. Zhao, M. Que, J. Chen and C. Yang, *J. Mater. Chem. C*, 2020, **8**, 16258–16281.